ACS Catalysis

pubs.acs.org/acscatalysis

Research Article

Self-Exfoliated Synthesis of Transition Metal Phosphate Nanolayers for Selective Aerobic Oxidation of Ethyl Lactate to Ethyl Pyruvate

Wei Zhang, Paula Oulego, Sandeep K. Sharma, Xiu-Lin Yang, Lain-Jong Li, Gadi Rothenberg, and N. Raveendran Shiju*

Cite This: *ACS Catal.* 2020, 10, 3958−3967

Read Online

ACCESS | Metrics & More | Article Recommendations | Supporting Information

ABSTRACT: Two-dimensional (2D) transition metal nanosheets are promising catalysts because of the enhanced exposure of the active species compared to their 3D counterparts. Here, we report a simple, scalable, and reproducible strategy to prepare 2D phosphate nanosheets by forming a layered structure in situ from phytic acid (PTA) and transition metal precursors. Controlled combustion of the organic groups of PTA results in interlayer carbon, which keeps the layers apart during the formation of phosphate, and the removal of this carbon results in ultrathin nanosheets with controllable layers. Applying this concept to vanadyl phosphate synthesis, we show that the method yields 2D ultrathin nanosheets of the orthorhombic β-form, exposing abundant V^{4+}/V^{5+} redox sites and oxygen vacancies. We demonstrate the high catalytic activity of this material in the vapor-phase aerobic oxidation of ethyl lactate to ethyl pyruvate. Importantly, these β-$VOPO_4$ compounds do not get hydrated, thereby reducing the competing hydrolysis reaction by water byproducts. The result has superior selectivity to ethyl pyruvate compared to analogous vanadyl phosphates. The catalysts are highly stable, maintaining a steady-state conversion of ~90% (with >80% selectivity) for at least 80 h on stream. This "self-exfoliated" synthesis protocol opens opportunities for preparing structurally diverse metal phosphates for catalysis and other applications.

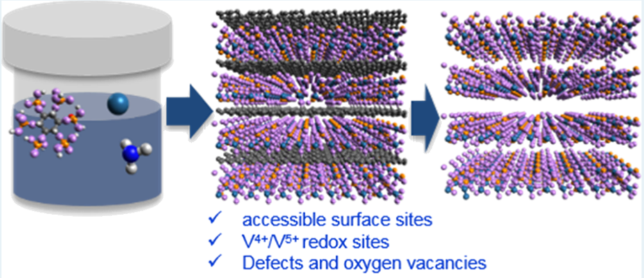

Spot on! A template-free strategy to prepare 2D phosphate nanosheets for selective aerobic oxidation.

KEYWORDS: *metal phosphate, β-phase, ultrathin nanosheets, heterogeneous catalysis, aerobic oxidation, lactic acid*

■ INTRODUCTION

Ultrathin two-dimensional (2D) materials are attracting increased attention for several applications, thanks to their distinctive electronic, optical, semiconducting, and catalytic properties.[1,2] Single- or few-layer 2D sheets expose more interior atoms than their bulk counterparts, with abundant surface-active sites and vacancy defects.[3,4] The 2D confinement effect also can shorten mass and heat diffusion pathways.[5] This makes them promising candidates for designing efficient heterogeneous catalysts.[6]

The main state-of-the-art methods for preparing few-layer nanosheets are gas/liquid exfoliation, ion intercalation, or mechanical cleavage.[7] These top-down approaches are suitable for stacked materials with interplanar van der Waals interactions, such as graphene, boron nitride, and carbon nitride.[8] Synthesizing 2D nanosheets from nonlayered materials is much more difficult.[9] It requires harsh conditions and gives varied thicknesses and low yields.[10] Alternatively, 2D nonlayered nanosheets can be produced through template-assisted synthesis,[11,12] surfactant self-assembly,[13,14] oriented attachment growth,[15] and inorganic−organic lamellar hybrid intermediates.[16] Still, making high-quality ultrathin nanosheets of nonlayered inorganic materials remains a challenge.[17,18]

For example, vanadium phosphates (VPOs) are composed of alternating vanadium octahedra (VO_6) and phosphate tetrahedra (PO_4).[19] Several crystal structures in different oxidation states are known, such as V^{5+} vanadyl phosphate (i.e., α_I-, α_{II}-, β-, ω-, δ-, ε-, and γ-V^VOPO_4) and V^{4+} vanadyl pyrophosphate [$(V^{IV}O)_2P_2O_7$].[20−24] The β-phase is thermodynamically the most stable.[25] However, because this compact structure has fewer accessible active sites, its catalytic activity is low.[26] We hypothesized that this problem could be avoided by structuring β-$VOPO_4$ as thin nanosheets, thus exposing more surface V^{4+}/V^{5+} redox couples.[27] $VOPO_4$ nanosheets are currently prepared by intercalation−exfoliation of bulk α-$VOPO_4 \cdot 2H_2O$, exploiting the weak hydrogen bonds between layers.[28] However, unlike layered α-$VOPO_4$, the 3D network of the nonlayered β-phase is unsuitable for this method, giving no control over the number of layers.

Received: October 15, 2019
Revised: February 17, 2020
Published: February 19, 2020

https://dx.doi.org/10.1021/acscatal.9b04452
ACS Catal. 2020, 10, 3958−3967

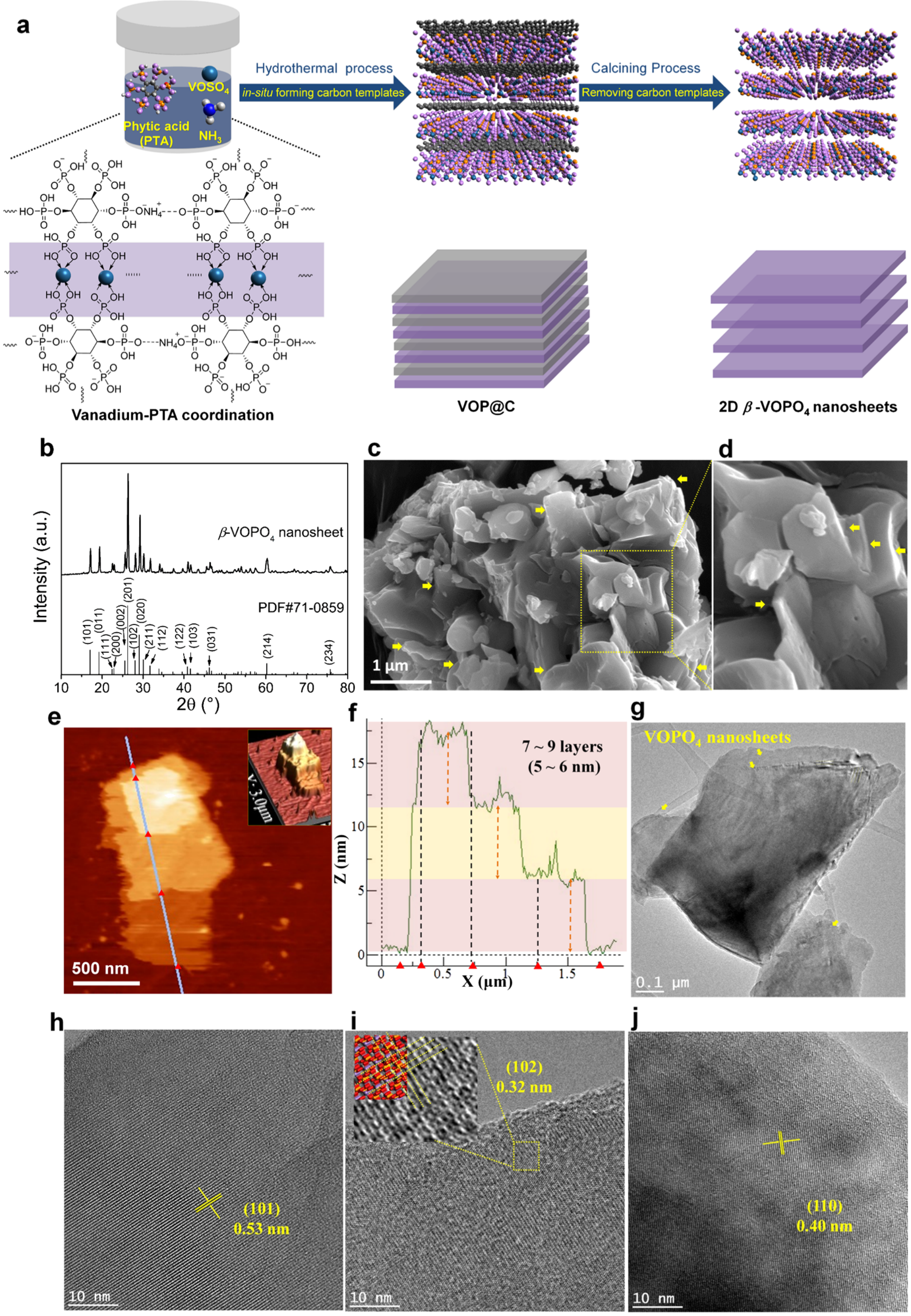

Figure 1. (a) Schematic summary of the synthesis procedure for 2D β-$VOPO_4$ nanosheets. (b) X-ray diffraction pattern of 2D β-$VOPO_4$ nanosheets (the inset shows the model of layered β-$VOPO_4$); (c,d) SEM images of β-$VOPO_4$ flakes stacked by the layered structure; (e) AFM image of few-layer β-$VOPO_4$ nanosheets (inset: the corresponding 3D demonstration); (f) thickness of nanosheets derived from AFM measurement; (g) representative TEM images of β-$VOPO_4$ nanosheets; and (h−j) magnified HRTEM images of β-$VOPO_4$ nanosheets taken along [101], [102], and [110] directions.

Here, we report a new template-free and scalable method for preparing 2D β-$VOPO_4$ ultrathin nanosheets with controlled layers. These sheets are made by self-assembly of vanadyl sulfate ($VOSO_4$) and phytic acid (PTA) precursors, which are abundant and inexpensive; vanadyl sulfate is a byproduct of crude oil refining, and PTA is a renewable plant-based acid. The PTA molecules are the key to this synthesis: (i) they react with $VOSO_4$ as strong chelating agents, suppressing the

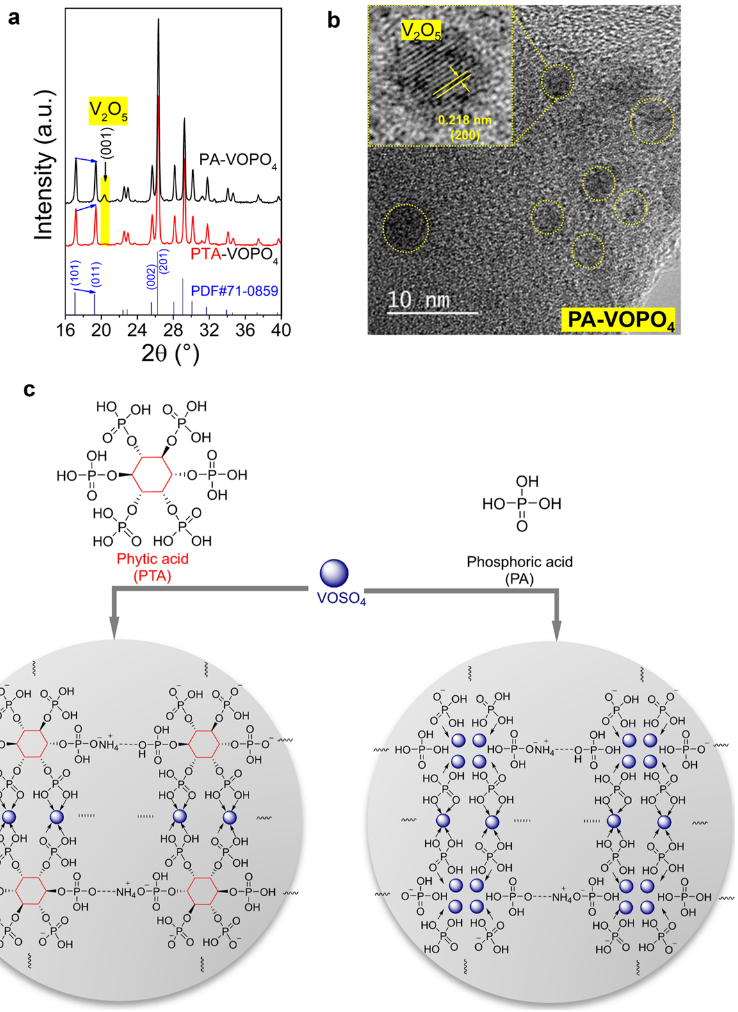

Figure 2. (a) Comparison of the X-ray diffraction patterns of two β-VOPO$_4$ catalysts: phytic acid-derived VOPO$_4$ nanosheets (PTA−VOPO$_4$) and the corresponding phosphoric acid-derived VOPO$_4$ (PA−VOPO$_4$); (b) magnified HRTEM images of PA−VOPO$_4$, and the inset shows the V_2O_5 nanoparticles with the (200) lattice space. (c) Schematic of the self-assembly process of VOSO$_4$ and P precursors: PTA and phosphoric acid (PA).

agglomeration of vanadium species, and (ii) they form carbon layers between the vanadium−phosphate complexes from the cyclohexane rings during the hydrothermal process. Subsequent pyrolysis removes the PTA, creating more accessible surface and increasing the number of V^{4+}/V^{5+} redox sites and oxygen vacancies. This self-exfoliating concept is also general, giving access to various thin transition metal phosphate sheets. We used this method to make active and selective catalysts from inactive forms of phosphates by structuring them as thin nanosheets, thereby exposing more surface active species. The resulting 2D β-VOPO$_4$ ultrathin sheets are excellent catalysts for the vapor-phase air oxidation of ethyl lactate to ethyl pyruvate (Figure S1, see the Supporting Information for full experimental details).

■ RESULTS AND DISCUSSION

Synthesis and Characterization of β-VOPO$_4$ Nanosheets. Figure 1a illustrates the synthesis strategy for 2D β-VOPO$_4$ ultrathin sheets. In the first step of this simple two-step process, PTA and VOSO$_4$ are dissolved in aqueous solutions, separately. After mixing the two solutions, the vanadium−PTA coordination precursors are formed by the self-assembly of vanadyl ions and PTA. Subsequently, ammonia was added to the mixture, adjusting the pH to ~6. Adding ammonia accelerates the complexation and helps to form cross-linked networks by surrounding the vanadium−PTA micelles. The amorphous mixture is then subjected to a hydrothermal treatment (Figure S2). Then, the cyclohexane part of PTA is carbonized, forming VOP@C hybrids. Note that the growth of carbon was restricted between the interlayers of VOP−PTA hybrids, forming extended 2D carbon layers. In the second step, the in situ-formed carbon templates were removed by heat treatment at 550 °C, yielding 2D β-VOPO$_4$ nanosheets.

Powder X-ray diffraction analysis confirmed the formation of the pure orthorhombic β-VOPO$_4$ phase (Figure 1b, cf. PDF#71-0859). Scanning electron microscopy (SEM) images show the stacked 2D plates with a smooth surface, shaped edges and corners, indicating a typical lamellar layered morphology (Figure 1c,d). Analysis of the sample by atomic force microscopy (AFM) (Figures 1e and S3) and the corresponding AFM height profile (Figure 1f) indicate that the VOPO$_4$ samples comprise three stacks (see the inset in Figure 1e), each with the same average thickness of ~6 nm. This confirms that we successfully synthesized the β-VOPO$_4$ nanosheets with a controlled thickness of about 7−8 atomic monolayers. The ultrathin and nearly transparent features of VOPO$_4$ nanosheets are also shown by transmission electron microscopy (TEM) (Figure 1g), upholding the AFM results.

Moreover, the high-resolution TEM (HRTEM) images show the clear lattice fringes with interplanar distances of 0.53, 0.32, and 0.40 nm (Figure 1h–j), which can be assigned to the (101), (102), and (110) planes of the β-$VOPO_4$ structure, respectively.

We hypothesized that PTA plays a key role in the formation of 2D β-$VOPO_4$ nanosheets. To test this, we ran a control experiment, where instead of PTA, we used phosphoric acid (H_3PO_4) as the P precursor (all other conditions were identical). The resulting $VOPO_4$ material is denoted as PA–$VOPO_4$. As shown in Figure 2a, the XRD pattern of PA–$VOPO_4$ is almost identical to that of the PTA-derived $VOPO_4$ nanosheets (denoted as PTA–$VOPO_4$), yielding a typical β structure. Unlike layered α-$VOPO_4$ with 2D anisotropic growth (the adjacent layers are connected with weak van der Waals force),[28] diffraction peaks do not shift in the β-phase.[29] However, the ratios of both (011)/(101) and (002)/(201) planes in PTA–$VOPO_4$ are higher than those of PA–$VOPO_4$ (Figures 2a and S4), probably because of the lamellar layered structure of PTA–$VOPO_4$.

However, an additional peak appeared at 20.3° in PA–$VOPO_4$, which belongs to crystalline V_2O_5. This indicates that some of the vanadyl species are aggregated into V_2O_5. Indeed, a representative HRTEM image of PA–$VOPO_4$ (Figure 2b) confirmed that the V_2O_5 nanocrystallites are dispersed on the $VOPO_4$ matrix. The inset clearly shows lattice fringes of 0.218 nm, corresponding to the (200) lattice space of crystalline V_2O_5. The chemical mapping by energy-dispersive X-ray (EDX) spectroscopy showed that the mean atomic V/P ratio of surface PTA–$VOPO_4$ is 0.9 (Table S1), much lower than that of PA–$VOPO_4$ (1.41, see Table S2), indicating the aggregation of vanadia species on the surface of PA–$VOPO_4$.

Both PTA and phosphoric acid are strong chelating agents and coordinate to $VOSO_4$. As shown in Figure 2c, PTA comprises six phosphoric acids attached to a cyclohexane ring. Unlike plain phosphoric acid, the steric hindrance of PTA prevents aggregation during the co-assembly process. Moreover, during the hydrothermal treatment, the cyclohexane segments of PTAs are carbonized into a carbon framework, suppressing the agglomeration of vanadium species to V_2O_5. Indeed, after the hydrothermal treatment, the nitrogen sorption isotherm of PTA-derived VOP (PTA–VOP_{HT}) showed increased N_2 uptake in the low relative pressure ($P/P_0 < 0.1$) and a hysteresis loop in the region of $P/P_0 > 0.4$, suggesting the formation of a carbon rich in micropores and mesopores (Figure S5a). In contrast, the PA–VOP_{HT} gave negligible N_2 adsorption. Subsequent calcination removes the carbon, giving PTA–$VOPO_4$, showing a steep rise in the range of $P/P_0 > 0.9$ (Figure S5b), which can be assigned to the interlayer voids. We also prepared PA–$VOPO_4$ samples with different $VOSO_4$/PA molar ratios (0.5 and 0.8) under otherwise identical conditions, trying to avoid the formation of crystalline V_2O_5. As is evident from the XRD patterns in Figure S6 in the Supporting Information, crystalline V_2O_5 was present in these samples, further verifying the vital role of the PTA precursor. We conclude that owing to the confined carbonization of PTA, the formed carbon acts as an in situ template, giving the desired few-layer nanosheets. Control experiments wherein the vanadium–PTA complex was directly calcined without any hydrothermal treatment led to the formation of amorphous VPO (Figure S7), upholding our conclusion.

We then studied the catalytic performance of these β-$VOPO_4$ materials in the vapor-phase oxidative dehydrogenation of ethyl lactate with air to give ethyl pyruvate in a fixed-bed reactor (eq 1). Lactates are biomass-derived "platform molecules,"[30] and direct aerobic oxidation of lactate is a sustainable route to biobased pyruvate, an important intermediate in the food, cosmetics, pharmaceutical, and agrochemical sectors.[31,32] Previously, we showed that aerobic oxidation of ethyl lactate requires relatively high temperatures. However, the pyruvate is easily overoxidized on the catalyst surface at such high temperatures, lowering the product selectivity.[33] A series of control experiments confirmed that the reaction is in the kinetic regime, with no mass-transfer limitations. Then, we measured the selectivity to ethyl pyruvate against ethyl lactate conversion over phytic acid-derived $VOPO_4$ nanosheets (PTA–$VOPO_4$) and phosphoric acid-derived 3D $VOPO_4$ nanoparticles (PA–$VOPO_4$) (Figure 3a).

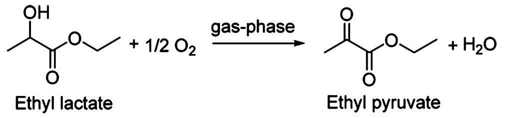

(1)

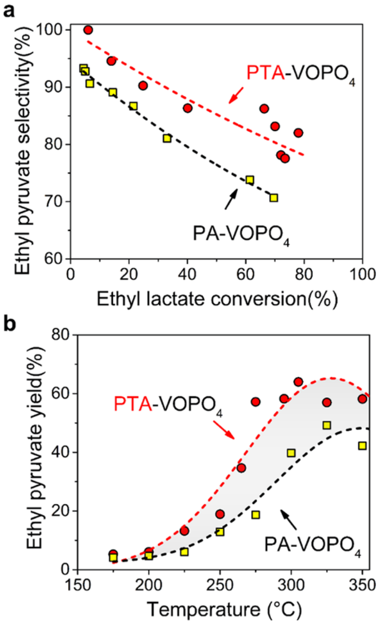

Figure 3. Vapor-phase oxidative dehydrogenation of ethyl lactate with air to give ethyl pyruvate over various β-$VOPO_4$ catalysts: (a) Selectivity to ethyl pyruvate plotted against conversion over PTA–$VOPO_4$ and PA–$VOPO_4$. Reaction conditions: ethyl lactate WHSV = 6.25 h^{-1}, air carrier flow rate = 2.25 L/h; (b) corresponding temperature-resolved yield profile of ethyl pyruvate. All data were taken after 2 h on stream.

PTA–$VOPO_4$ outperformed PA–$VOPO_4$ under identical reaction conditions. At the same conversion of ethyl lactate, PTA–$VOPO_4$ is more selective for ethyl pyruvate than PA–$VOPO_4$. The ethyl pyruvate yield at different reaction temperatures was much higher over PTA–$VOPO_4$ nanosheets (Figure 3b), confirming the enhanced catalytic activity. Previously, we demonstrated that this reaction is kinetically favored in the presence of isolated amorphous vanadium oxide sites, while crystalline V_2O_5 can catalyze this reaction but not selective.[34,35] PA–$VOPO_4$ features well-dispersed V_2O_5 nano-

https://dx.doi.org/10.1021/acscatal.9b04452

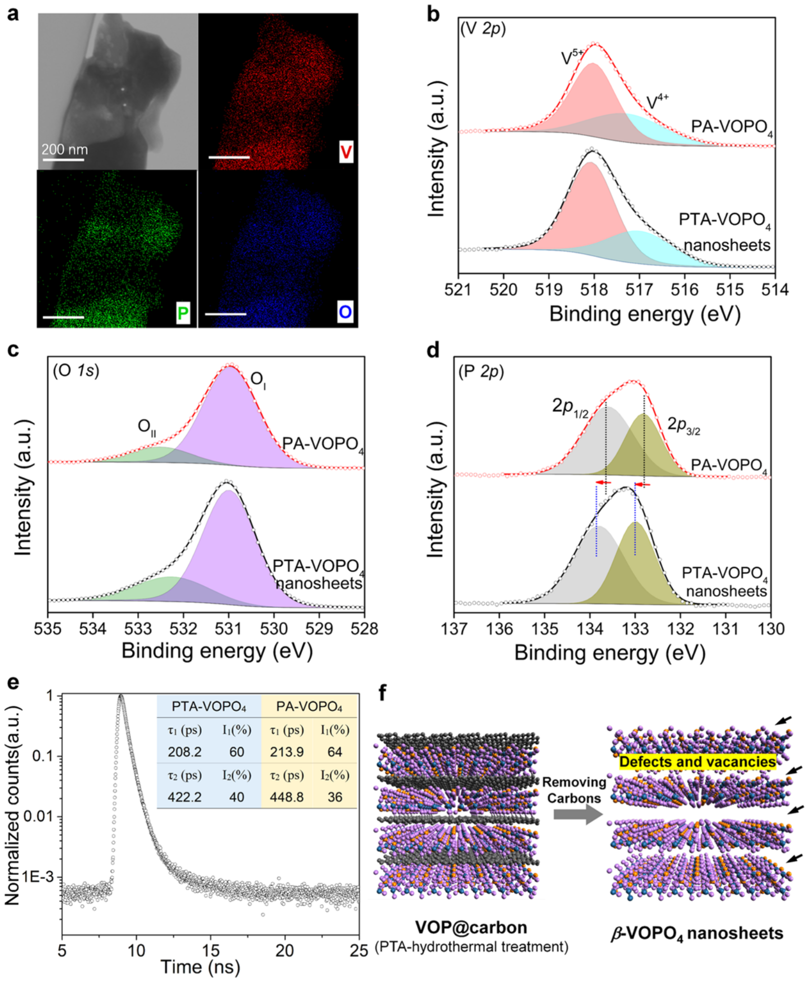

PTA-VOPO$_4$		PA-VOPO$_4$	
τ_1 (ps)	I_1(%)	τ_1 (ps)	I_1(%)
208.2	60	213.9	64
τ_2 (ps)	I_2(%)	τ_2 (ps)	I_2(%)
422.2	40	448.8	36

Figure 4. (a) STEM image and corresponding elemental mappings of V, P, and O of PTA−VOPO$_4$ nanosheets. XPS studies showing high-resolution V 2p spectra (b), high-resolution O 1s spectra (c), and high-resolution P 2p spectra (d) of PA−VOPO$_4$ and PTA−VOPO$_4$ nanosheets. (e) PALS spectra of PTA−VOPO$_4$ nanosheets (the inset shows the positron annihilation lifetimes and the corresponding intensities in PA−VOPO$_4$ and PTA−VOPO$_4$ nanosheets, respectively). (f) Schematic diagram of defects and vacancies, originating from the removal of carbon layers, in PTA−VOPO$_4$ nanosheets.

crystals on the surface, yet its catalytic activity and selectively are lower compared to that of PTA−VOPO$_4$. This is probably because the surface V^{4+}/V^{5+} active sites and oxygen vacancies of PA−VOPO$_4$ are less accessible than those in PTA−VOPO$_4$. We then reasoned that the reactivity enhancement on PTA−VOPO$_4$ is due to the exposed V^{4+}/V^{5+} redox sites and oxygen vacancies.

Factors Governing Activity and Selectivity. We further characterized the β-VOPO$_4$ sheets to understand this enhanced activity. The full X-ray photoelectron spectroscopy (XPS) survey spectra showed V, P, and O in all samples (Figure S8), in accordance with elemental mapping from high-angle annular dark-field scanning TEM (HAADF−STEM) analysis (Figures 4a and S9). As shown in Figure 4b, the spectra of V 2p can be deconvoluted into two peaks centered at 517.2 and 518.0 eV, which are associated with V^{4+} and V^{5+} species, respectively. The PTA−VOPO$_4$ nanosheets gave a much higher $V^{4+}/(V^{4+} + V^{5+})$ ratio of 40%, in comparison to 30% in the bulk PA−VOPO$_4$ material. Thus, ultrathin nanosheets expose more accessible surface sites, thereby increasing the number of surface V^{4+} species. The enhanced catalytic activity can be assigned to the increased V^{4+}/V^{5+} redox active sites of β-VOPO$_4$ nanosheets.[36] From redox perspectives, introducing V^{4+} into β-VOPO$_4$ nanosheets increases the number of defects and oxygen vacancies. Elsewhere, we have reported that the oxidation of ethyl lactate follows a Mars−van Krevelen mechanism: ethyl lactate adsorbed on the catalytic surface is oxidized by the lattice oxygen, and then, the resultant oxygen vacancies are replenished by gas-phase oxygen during the oxidation reaction.[33] Thus, both surface lattice oxygens and oxygen vacancies play key roles in aerobic oxidation of ethyl lactate to ethyl pyruvate. These two species can be roughly estimated from the O 1s XPS spectrum (Figure 4c): the peak at ∼532.5 eV can be attributed to the lattice oxygen (O_I) and the peak at ∼531.0 eV can be attributed to the adsorbed oxygen species at the vacancy sites (O_{II}).[4] The O_I peak has a larger area for the PTA−VOPO$_4$ nanosheets than PA−VOPO$_4$, indicating that the former exposes more lattice oxygen atoms. Additionally, O_{II} oxygens can enhance the mobility of oxygen species; they are more easily reduced and favorable for the oxidation reaction. PTA−VOPO$_4$ has a higher $O_{II}/(O_I + O_{II})$ ratio, indicating abundant structural defects and oxygen vacancies. Moreover, as the structural defects and oxygen vacancies decrease the electron charge density around phosphorus of PTA−VOPO$_4$, the P $2p_{1/2}$ and P $2p_{3/2}$ peaks shift slightly

https://dx.doi.org/10.1021/acscatal.9b04452
ACS Catal. 2020, 10, 3958−3967

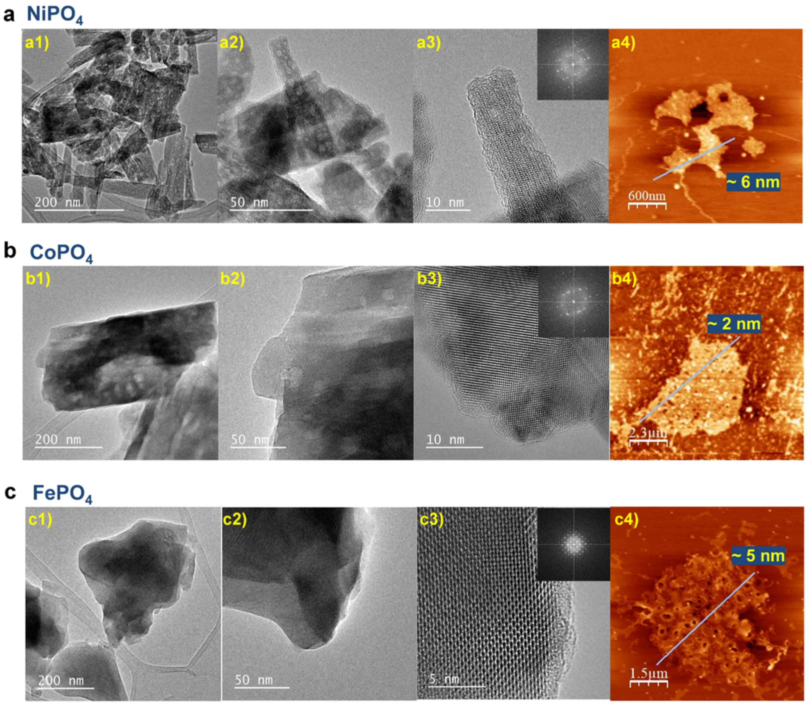

Figure 5. Morphological and microstructural characterization of various PTA-derived metal-phosphate nanosheets (a−c); $NiPO_4$ nanosheets: (a1−a3) TEM images and (a4) AFM image; $CoPO_4$ nanosheets: (b1−b3) TEM images and (b4) AFM image; $FePO_4$ nanosheets: (c1−c3) TEM images and (c4) AFM image. Note: the corresponding height profiles of phosphate nanosheets are shown in Figure S11, which were derived from AFM measurement.

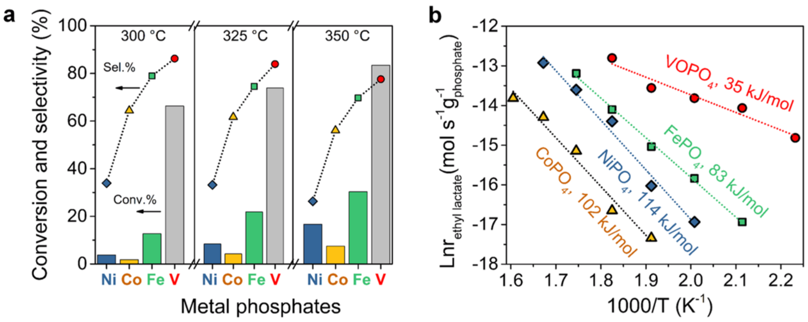

Figure 6. (a) Comparisons of ethyl lactate conversion and ethyl pyruvate selectivity over various PTA-derived metal phosphate nanosheets: $VOPO_4$, $FePO_4$, $CoPO_4$, and $NiPO_4$. Reaction conditions: ethyl lactate WHSV = 8 h^{-1}, air flow rate = 2.25 L/h, and reaction temperature: 300, 325, and 350 °C. (b) Arrhenius plots for steady-state ethyl lactate consumption rate over various phosphate catalysts, and the apparent activation energy (E_a) was measured at a series of temperatures below 15% ethyl lactate conversion.

toward a higher binding energy in comparison with PA−$VOPO_4$ (Figure 4d).[37]

Further information on the structural defects was obtained from positron annihilation lifetime spectroscopy (PALS). Figure 4e shows a typical PALS spectrum of PTA−$VOPO_4$. All the PALS spectra could be fitted to two positron lifetime components with a reasonable variance of fit (1.0−1.1). The first positron lifetime (τ_1) in the range of ~208−240 ps is attributed to positron annihilation in the bulk of the materials (see the inset in Figure 4e). The longer lifetime (τ_2) in the range of ~422−478 ps indicates the presence of larger-size defects, that is, vacancy clusters present either in the bulk or at the grain boundaries of the samples. The τ_1 values of PTA−$VOPO_4$ and PA−$VOPO_4$ are nearly the same, showing the identical lattice structure. The intensity corresponding to larger components (I_2) is higher (40%) for nanosheets compared to that of bulk PA−$VOPO_4$ (36%), suggesting more vacancy defects for PTA−$VOPO_4$ nanosheets. Positrons trapped at the defect sites predominantly annihilate with the surrounding elements and hence provide information about the chemical surrounding. They are efficiently trapped either at negatively charged or neutral open volume defects such as vacancy clusters. According to the crystal structure of the samples, cation vacancy defects (e.g., V or P based vacancy defects) are surrounded by oxygen atoms. Figure S10 shows the ratio curves of these samples with respect to a reference Si, in which the peak at $P_L \approx 10 \times 10^{-3}\ m_oc$ indicates the annihilation with the surrounding oxygen atoms at the defect sites. The corresponding peak intensity of PTA−$VOPO_4$ is higher than that of PA−$VOPO_4$, indicating that the defects present in the nanosheets have more O atoms in the surrounding lattice sites. Thus, our ultrathin $VOPO_4$ nanosheets expose more lattice oxygen and oxygen vacancies (Figure 4f), which can explain their high catalytic activity.

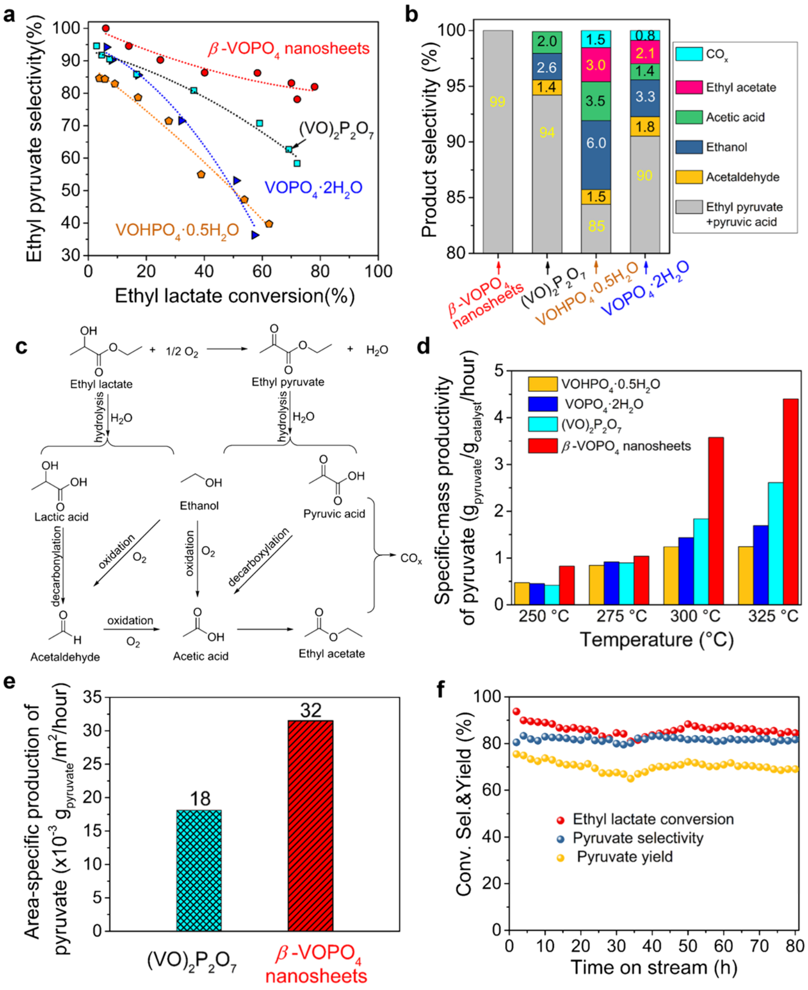

Figure 7. (a) Selectivity to ethyl pyruvate plotted against conversion for different VPO catalysts: 2D β-$VOPO_4$ nanosheets, $(VO)_2P_2O_7$, $VOHPO_4\cdot 0.5\ H_2O$, and $VOPO_4\cdot 2H_2O$. (b) Comparison of the selectivity of various products at an ethyl lactate conversion of ∼6% (β-$VOPO_4$ nanosheets: 6.0%, $(VO)_2P_2O_7$: 6.2%, $VOHPO_4\cdot 0.5\ H_2O$: 5.7%, and $VOPO_4\cdot 2H_2O$: 6.4%). The carbon balances were >98%. (c) Reaction pathway for the aerobic oxidation of ethyl lactate on the VPO catalysts. (d) Mass-specific activity for pyruvate formation over VPO catalysts in the temperature range 250−325 °C. (e) Comparisons of the area-specific production rate of pyruvate over 2D β-$VOPO_4$ nanosheets and $(VO)_2P_2O_7$. (f) Stability test of the 2D β-$VOPO_4$ nanosheets under optimized conditions (WHSV = 3 h^{-1} and T = 300 °C).

Self-Exfoliated Synthesis of Other Transition Metal Phosphate Nanolayers for Catalytic Aerobic Oxidation of Ethyl Lactate to Ethyl Pyruvate. Based on this "self-exfoliated" synthesis protocol, we successfully made V-, Ni-, Co-, and Fe-based phosphates (see the experimental section in the Supporting Information for details). These desired few-layer nanosheets with thicknesses of 2−6 nm were confirmed by HRTEM and AFM analyses (Figures 5a−c and S11). The combination of XRD, SEM, and EDX analyses showed that these phosphates have lamellar layered morphologies with high crystallinity, purity, and uniformity (Figures S12 and S13 and Tables S3−S5, in the Supporting Information). Thus, our synthesis method is general, facile, and scalable via a two-step process (hydrothermal and calcination treatment).

All the PTA-derived phosphate nanosheets were then tested in the vapor-phase aerobic oxidation of ethyl lactate with air at different reaction temperatures (300, 325, and 350 °C). As shown in Figure 6a, control experiments confirmed that Ni and Co showed some conversion but selectivity to ethyl pyruvate was low, owing to the hydrolysis of ethyl pyruvate on Co- and Ni-based phosphate.[36] Intriguingly, $VOPO_4$ nanosheets exhibited the best catalytic performance among all the phosphate catalysts tested in this study, giving a remarkably high activity and selectivity. To better understand this, the apparent activation energies (E_a) were calculated based on Arrhenius plots (Figure 6b), from the data collected below 15% ethyl lactate conversion. The corresponding E_a value for $VOPO_4$ (35 kJ/mol) is much smaller than that for other phosphates: $FePO_4$ (83 kJ/mol), $CoPO_4$ (102 kJ/mol), and $NiPO_4$ (114 kJ/mol). This result confirmed that $VOPO_4$ is intrinsically more active for ethyl lactate oxidation.

Comparisons of Catalytic Efficiency of Various Vanadium Phosphorus Oxides for Aerobic Oxidation to Ethyl Lactate. Olier et al. reported that all vanadium phosphorus oxides (VPO) can be hydrated except for β-$VOPO_4$, owing to its highly stable structure.[38] This is consistent with our XPS measurements (Figure 4c), where no surface-chemisorbed water was detected (∼533 eV). As a result, the competing hydrolysis is suppressed, which may explain why the β-$VOPO_4$ nanosheets gave such high selectivity to pyruvate compared with other metal phosphate catalysts.

To test this, we prepared a series of bulk VPO catalysts for comparison with our nanosheets: vanadyl pyrophosphate

[$(VO)_2P_2O_7$], vanadyl phosphate dihydrate ($VOPO_4·2H_2O$), and vanadyl hydrogen phosphate hemihydrate ($VOHPO_4·0.5H_2O$, see the Supporting Information for full experimental details). Their crystalline structures were confirmed by XRD and Raman spectroscopy (Figures S14 and S15).[39,40] Figure 7a shows the selectivity−conversion plots. All the VPO catalysts were active in lactate-to-pyruvate reaction. Interestingly, β-$VOPO_4$ nanosheets showed the highest ethyl pyruvate selectivity, reaching over 90% at an ethyl lactate conversion of ∼25%. Even at a high ethyl lactate conversion of ∼80%, the selectivity is as high as 80% compared with ∼60% for $(VO)_2P_2O_7$. Control experiments were performed at a steady-state conversion of ∼6% for all the tested catalysts (the carbon balances were >98%) to better differentiate the influence of the VPO phases on product selectivity. As shown in Figure 7b, β-$VOPO_4$ nanosheets gave over 99% selectivity to ethyl pyruvate, while a series of byproducts were detected on other three VPO catalysts, such as acetaldehyde, ethanol, acetic acid, ethyl acetate, and CO_x. This indicates that except for the β-phase, the VPO catalysts undergo the competing overoxidation, hydrolysis, decarbonylation, and decarboxylation (see Figure 7c). The byproduct distribution is different among different catalysts. $VOHPO_4·0.5H_2O$ and $VOPO_4·2H_2O$ gave higher selectivity to ethanol than $(VO)_2P_2O_7$, owing to the hydrolysis of ester on their hydrated surfaces.

We also compared the mass-specific activity (calculated as grams of pyruvate produced per gram of the catalyst per hour) over VPO catalysts at different temperatures (Figure 7d). Our β-$VOPO_4$ catalyst outperformed the classical phosphates, especially at high reaction temperatures over 300 °C. Moreover, layered β-$VOPO_4$ and $(VO)_2P_2O_7$ gave similar specific Brunauer−Emmett−Teller areas of 33 and 25 m^2/g, respectively, much higher than $VOHPO_4·0.5H_2O$ (16 m^2/g), $VOPO_4·2H_2O$ (9 m^2/g). We then plotted the area-specific catalytic rates for pyruvate production over β-$VOPO_4$ and $(VO)_2P_2O_7$ catalysts. As shown in Figure 7e, the area-specific activity for β-$VOPO_4$ nanosheets is almost twice higher than that for $(VO)_2P_2O_7$ at 300 °C. The stability and regenerability are key factors for a heterogenous catalyst in its practical application. We tested the stability of our β-$VOPO_4$ nanosheets under optimized conditions (WHSV = 3 h^{-1}, T = 300 °C, see Table S6). As shown in Figure 7f, this catalyst is highly stable, with a steady-state conversion of ∼90% (over 80% selectivity) for at least 80 h without significant loss of activity. We also used the same catalyst bed for a series of testing studies, and for this, the catalyst was cleaned and regenerated by simply passing air at 500 °C for 2 h and switching off the ethyl lactate feed. The XRD, TEM, and XPS analyses further confirmed that the structure was well preserved after multiple regenerations (Figures S16−S18 in the Supporting Information). Most of the 2D nanosheets are still far from commercialization because their cost is a problem to scale-up. Our 2D β-$VOPO_4$ nanosheets are promising in this regard because they can be readily achieved from inexpensive starting materials such as $VOSO_4$ and PTA. $VOSO_4$ is a byproduct of crude oil refining (ca. 2000−5000 \$/ton), and PTA is a renewable inexpensive plant-based acid (ca. 6500 \$/ton).[41] The metal salts are also cheap; therefore, these nanosheets are industrially viable catalysts cost-wise as well.

CONCLUSIONS

We report the synthesis of 2D ultrathin phosphate nanosheets by a new template-free "self-exfoliated" strategy using renewable PTA. PTA acts as a strong chelating agent, but can also be carbonized in situ into carbon templates, which are responsible for the precisely controlled few-layer nanosheets. Application of this method to VPO produces β-$VOPO_4$ ultrathin nanosheets, which expose abundant V^{4+}/V^{5+} redox sites and oxygen vacancies. Importantly, β-$VOPO_4$ does not get hydrated, thereby reducing the competing hydrolysis by water byproducts. These features result in a superior catalytic activity and selectivity in the aerobic oxidation of ethyl lactate to ethyl pyruvate compared to the classical VPO. The inexpensive β-$VOPO_4$ nanosheets show good long-term stability and facile recovery. These nanosheets are not only among the best heterogeneous catalysts for the vapor-phase oxidation of lactate to pyruvate, they also show for the first time that the "inert" β-$VOPO_4$ phase can be an efficient oxidation catalyst under the right conditions. Note that this is a general synthesis method, giving access to various metal phosphate nanosheets, such as Ni, Co, and Fe. Therefore, this work opens a new avenue for the synthesis of new transition metal phosphate nanosheets for catalysis and other applications.

ASSOCIATED CONTENT

Supporting Information

The Supporting Information is available free of charge at https://pubs.acs.org/doi/10.1021/acscatal.9b04452.

> Experimental procedures; additional characterization data of vanadyl phosphate catalysts including XRD patterns, nitrogen adsorption−desorption isotherms, SEM/TEM/AFM images, EDX spectra, XPS spectra, PALS spectra, and Raman spectra; and results of reaction parameters on aerobic oxidation of ethyl lactate with air (PDF)

AUTHOR INFORMATION

Corresponding Author

N. Raveendran Shiju − *Van 't Hoff Institute for Molecular Sciences, University of Amsterdam, 1098 XH Amsterdam, The Netherlands;* orcid.org/0000-0001-7943-5864;
Email: n.r.shiju@uva.nl

Authors

Wei Zhang − *Van 't Hoff Institute for Molecular Sciences, University of Amsterdam, 1098 XH Amsterdam, The Netherlands;* orcid.org/0000-0003-4506-6583
Paula Oulego − *Department of Chemical and Environmental Engineering, University of Oviedo, E-33071 Oviedo, Spain*
Sandeep K. Sharma − *Radiochemistry Division, Bhabha Atomic Research Centre, 400 085 Mumbai, India;* orcid.org/0000-0002-9285-3793
Xiu-Lin Yang − *Physical Sciences and Engineering Division, King Abdullah University of Science and Technology, 23955-6900 Thuwal, Kingdom of Saudi Arabia;* orcid.org/0000-0003-2642-4963
Lain-Jong Li − *Physical Sciences and Engineering Division, King Abdullah University of Science and Technology, 23955-6900 Thuwal, Kingdom of Saudi Arabia;* orcid.org/0000-0002-4059-7783
Gadi Rothenberg − *Van 't Hoff Institute for Molecular Sciences, University of Amsterdam, 1098 XH Amsterdam, The Netherlands*

Complete contact information is available at:

https://pubs.acs.org/10.1021/acscatal.9b04452

Notes

The authors declare no competing financial interest.

■ ACKNOWLEDGMENTS

W.Z. thanks the China Scholarship Council (201506140058) for a PhD fellowship. P.O. thanks the Spanish Ministry of Economy and Competitiveness (MINECO) (Project CTM2015-63864-R) and the European Union (FEDER) for funding. P.O. also thanks the access and technical assistance from the Scientific-Technical Services of the University of Oviedo. This work is part of the Research Priority Area Sustainable Chemistry of the University of Amsterdam, http://suschem.uva.nl.

■ REFERENCES

(1) Chhowalla, M.; Shin, H. S.; Eda, G.; Li, L.-J.; Loh, K. P.; Zhang, H. The chemistry of two-dimensional layered transition metal dichalcogenide nanosheets. *Nat. Chem.* **2013**, *5*, 263−275.

(2) Ling, T.; Wang, J.-J.; Zhang, H.; Song, S.-T.; Zhou, Y.-Z.; Zhao, J.; Du, X.-W. Freestanding Ultrathin Metallic Nanosheets: Materials, Synthesis, and Applications. *Adv. Mater.* **2015**, *27*, 5396−5402. Gitis, V.; Chung, S.-H.; Shiju, N. R. Conversion of furfuryl alcohol into butyl levulinate with graphite oxide and reduced graphite oxide. *FlatChem* **2018**, *10*, 39.

(3) Hong, J.; Jin, C.; Yuan, J.; Zhang, Z. Atomic Defects in Two-Dimensional Materials: From Single-Atom Spectroscopy to Functionalities in Opto-/Electronics, Nanomagnetism, and Catalysis. *Adv. Mater.* **2017**, *29*, 1606434.

(4) Zhang, B.; Wang, L.; Zhang, Y.; Ding, Y.; Bi, Y. Ultrathin FeOOH Nanolayers with Rich Oxygen Vacancies on BiVO4 Photoanodes for Efficient Water Oxidation. *Angew. Chem., Int. Ed.* **2018**, *57*, 2248−2252.

(5) Xiong, P.; Ma, R.; Sakai, N.; Sasaki, T. Genuine Unilamellar Metal Oxide Nanosheets Confined in a Superlattice-like Structure for Superior Energy Storage. *ACS Nano* **2018**, *12*, 1768−1777.

(6) Ng, W. H. K.; Gnanakumar, E. S.; Batyrev, E.; Sharma, S. K.; Pujari, P. K.; Greer, H. F.; Zhou, W.; Sakidja, R.; Rothenberg, G.; Barsoum, M. W.; Shiju, N. R. The Ti3 AlC2 MAX Phase as an Efficient Catalyst for Oxidative Dehydrogenation of n-Butane. *Angew. Chem., Int. Ed.* **2018**, *57*, 1485−1490.

(7) Yang, W.; Zhang, X.; Xie, Y. Advances and challenges in chemistry of two-dimensional nanosheets. *Nano Today* **2016**, *11*, 793−816.

(8) Geim, A. K.; Grigorieva, I. V. Van der Waals heterostructures. *Nature* **2013**, *499*, 419.

(9) Di, J.; Xia, J.; Li, H.; Liu, Z. Freestanding atomically-thin two-dimensional materials beyond graphene meeting photocatalysis: Opportunities and challenges. *Nano Energy* **2017**, *35*, 79−91.

(10) Zhu, W.; Gao, X.; Li, Q.; Li, H.; Chao, Y.; Li, M.; Mahurin, S. M.; Li, H.; Zhu, H.; Dai, S. Controlled Gas Exfoliation of Boron Nitride into Few-Layered Nanosheets. *Angew. Chem., Int. Ed.* **2016**, *55*, 10766−10770.

(11) Huang, X.; Li, S.; Huang, Y.; Wu, S.; Zhou, X.; Li, S.; Gan, C. L.; Boey, F.; Mirkin, C. A.; Zhang, H. Synthesis of hexagonal close-packed gold nanostructures. *Nat. Commun.* **2011**, *2*, 292.

(12) Cheng, W.; He, J.; Yao, T.; Sun, Z.; Jiang, Y.; Liu, Q.; Jiang, S.; Hu, F.; Xie, Z.; He, B.; Yan, W.; Wei, S. Half-Unit-Cell α-Fe_2O_3 Semiconductor Nanosheets with Intrinsic and Robust Ferromagnetism. *J. Am. Chem. Soc.* **2014**, *136*, 10393−10398.

(13) Wang, J.; Xu, Y.; Ding, B.; Chang, Z.; Zhang, X.; Yamauchi, Y.; Wu, K. C.-W. Confined Self-Assembly in Two-Dimensional Interlayer Space: Monolayered Mesoporous Carbon Nanosheets with In-Plane Orderly Arranged Mesopores and High Graphitized Framework. *Angew. Chem., Int. Ed.* **2018**, *57*, 2894−2898.

(14) Sun, Z.; Liao, T.; Dou, Y.; Hwang, S. M.; Park, M.-S.; Jiang, L.; Kim, J. H.; Dou, S. X. Generalized self-assembly of scalable two-dimensional transition metal oxide nanosheets. *Nat. Commun.* **2014**, *5*, 3813.

(15) Schliehe, C.; Juarez, B. H.; Pelletier, M.; Jander, S.; Greshnykh, D.; Nagel, M.; Meyer, A.; Foerster, S.; Kornowski, A.; Klinke, C.; Weller, H. Ultrathin PbS Sheets by Two-Dimensional Oriented Attachment. *Science* **2010**, *329*, 550−553.

(16) Son, J. S.; Wen, X.-D.; Joo, J.; Chae, J.; Baek, S.-i.; Park, K.; Kim, J. H.; An, K.; Yu, J. H.; Kwon, S. G.; Choi, S.-H.; Wang, Z.; Kim, Y.-W.; Kuk, Y.; Hoffmann, R.; Hyeon, T. Large-Scale Soft Colloidal Template Synthesis of 1.4 nm Thick CdSe Nanosheets. *Angew. Chem., Int. Ed.* **2009**, *48*, 6861−6864.

(17) Wang, F.; Wang, Z.; Shifa, T. A.; Wen, Y.; Wang, F.; Zhan, X.; Wang, Q.; Xu, K.; Huang, Y.; Yin, L.; Jiang, C.; He, J. Two-Dimensional Non-Layered Materials: Synthesis, Properties and Applications. *Adv. Funct. Mater.* **2017**, *27*, 1603254.

(18) Dou, Y.; Zhang, L.; Xu, X.; Sun, Z.; Liao, T.; Dou, S. X. Atomically thin non-layered nanomaterials for energy storage and conversion. *Chem. Soc. Rev.* **2017**, *46*, 7338−7373.

(19) Centi, G.; Trifiro, F.; Ebner, J. R.; Franchetti, V. M. Mechanistic aspects of maleic anhydride synthesis from C4 hydrocarbons over phosphorus vanadium oxide. *Chem. Rev.* **1988**, *88*, 55−80.

(20) Weng, W.; Al Otaibi, R.; Alhumaimess, M.; Conte, M.; Bartley, J. K.; Dummer, N. F.; Hutchings, G. J.; Kiely, C. J. Controlling vanadium phosphate catalyst precursor morphology by adding alkane solvents in the reduction step of $VOPO_4 \cdot 2H_2O$ to $VOHPO_4 \cdot 0.5H_2O$. *J. Mater. Chem.* **2011**, *21*, 16136−16146.

(21) Centi, G. Vanadyl Pyrophosphate - A Critical Overview. *Catal. Today* **1993**, *16*, 5−26.

(22) Coulston, G. W.; Bare, S. R.; Kung, H.; Birkeland, K.; Bethke, G. K.; Harlow, R.; Herron, N.; Lee, P. L. The Kinetic Significance of V^{5+} in n-Butane Oxidation Catalyzed by Vanadium Phosphates. *Science* **1997**, *275*, 191−193.

(23) Hutchings, G. J.; Desmartin-Chomel, A.; Olier, R.; Volta, J.-C. Role of the product in the transformation of a catalyst to its active state. *Nature* **1994**, *368*, 41.

(24) Lashier, M.; Schrader, G. L. Reactive lattice oxygen sites for C4 hydrocarbon selective oxidation over β-$VOPO_4$. *J. Catal.* **1991**, *128*, 113−125.

(25) Gopal, R.; Calvo, C. Crystal structure of β VPO_5. *J. Solid State Chem.* **1972**, *5*, 432−435.

(26) Willinger, M. G.; Su, D. S.; Schlögl, R. Electronic structure of β-$VOPO_4$. *Phys. Rev. B: Condens. Matter Mater. Phys.* **2005**, *71*, 155118.

(27) Eichelbaum, M.; Hävecker, M.; Heine, C.; Karpov, A.; Dobner, C.-K.; Rosowski, F.; Trunschke, A.; Schlögl, R. The Intimate Relationship between Bulk Electronic Conductivity and Selectivity in the Catalytic Oxidation of n-Butane. *Angew. Chem., Int. Ed.* **2012**, *51*, 6246−6250.

(28) Wu, C.; Lu, X.; Peng, L.; Xu, K.; Peng, X.; Huang, J.; Yu, G.; Xie, Y. Two-dimensional vanadyl phosphate ultrathin nanosheets for high energy density and flexible pseudocapacitors. *Nat. Commun.* **2013**, *4*, 2431.

(29) Zhang, Y.; Zhang, X.; Ling, Y.; Li, F.; Bond, A. M.; Zhang, J. Controllable synthesis of few-layer bismuth subcarbonate by electrochemical exfoliation for enhanced CO_2 reduction performance. *Angew. Chem., Int. Ed.* **2018**, *57*, 13283−13287.

(30) Beerthuis, R.; Rothenberg, G.; Shiju, N. R. Catalytic routes towards acrylic acid, adipic acid and ε-caprolactam starting from biorenewables. *Green Chem.* **2015**, *17*, 1341−1361.

(31) Xu, P.; Qiu, J.; Gao, C.; Ma, C. Biotechnological routes to pyruvate production. *J. Biosci. Bioeng.* **2008**, *105*, 169−175.

(32) Sugiyama, S.; Kikumoto, T.; Tanaka, H.; Nakagawa, K.; Sotowa, K.-I.; Maehara, K.; Himeno, Y.; Ninomiya, W. Enhancement of Catalytic Activity on Pd/C and Te−Pd/C During the Oxidative Dehydrogenation of Sodium Lactate to Pyruvate in an Aqueous Phase Under Pressurized Oxygen. *Catal. Lett.* **2009**, *131*, 129−134.

(33) Zhang, W.; Innocenti, G.; Ferbinteanu, M.; Ramos-Fernandez, E. V.; Sepulveda-Escribano, A.; Wu, H.; Cavani, F.; Rothenberg, G.; Shiju, N. R. Understanding the oxidative dehydrogenation of ethyl lactate to ethyl pyruvate over vanadia/titania catalysts. *Catal. Sci. Technol.* **2018**, *8*, 3737−3747.

(34) Zhang, W.; Ensing, B.; Rothenberg, G.; Raveendran Shiju, N. Designing effective solid catalysts for biomass conversion: Aerobic oxidation of ethyl lactate to ethyl pyruvate. *Green Chem.* **2018**, *20*, 1866−1873.

(35) Zhang, W.; Oulego, P.; Slot, T. K.; Rothenberg, G.; Shiju, N. R. Selective Aerobic Oxidation of Lactate to Pyruvate Catalyzed by Vanadium-Nitrogen-Doped Carbon Nanosheets. *ChemCatChem* **2019**, *11*, 3381−3387.

(36) Zhang, W.; Innocenti, G.; Oulego, P.; Gitis, V.; Wu, H.; Ensing, B.; Cavani, F.; Rothenberg, G.; Shiju, N. R. Highly selective oxidation of ethyl lactate to ethyl pyruvate catalysed by mesoporous vanadia−titania. *ACS Catal.* **2018**, *8*, 2365−2374.

(37) Majjane, A.; Chahine, A.; Et-tabirou, M.; Echchahed, B.; Do, T.-O.; Breen, P. M. X-ray photoelectron spectroscopy (XPS) and FTIR studies of vanadium barium phosphate glasses. *Mater. Chem. Phys.* **2014**, *143*, 779−787.

(38) Benabdelouahab, G. F.; Volta, J. C.; Olier, R. New Insights into VOPO4 Phases Through Their Hydration. *J. Catal.* **1994**, *148*, 334−340.

(39) Li, X.; Ko, J.; Zhang, Y. Highly Efficient Gas-Phase Oxidation of Renewable Furfural to Maleic Anhydride over Plate Vanadium Phosphorus Oxide Catalyst. *ChemSusChem* **2018**, *11*, 612−618.

(40) Wang, F.; Dubois, J.-L.; Ueda, W. Catalytic dehydration of glycerol over vanadium phosphate oxides in the presence of molecular oxygen. *J. Catal.* **2009**, *268*, 260−267.

(41) Samotus, B.; Schwimmer, S. Phytic Acid as a Phosphorus Reservoir in the Developing Potato Tuber. *Nature* **1962**, *194*, 578.

Supporting Information

Self-exfoliated Synthesis of Transition Metal Phosphate Nanolayers for Selective Aerobic Oxidation of Ethyl Lactate to Ethyl Pyruvate

*Wei Zhang, [1] Paula Oulego, [2] Sandeep K Sharma,[3] Xiu-Lin Yang,[4] Lain-Jong Li,[4] Gadi Rothenberg [1] and N. Raveendran Shiju [1]**

[1] Van 't Hoff Institute for Molecular Sciences, University of Amsterdam, Science Park 904, 1098 XH Amsterdam, The Netherlands. *E-mail: n.r.shiju@uva.nl.

[2]Department of Chemical and Environmental Engineering, University of Oviedo, C/ Julián Clavería, s/n. E-33071, Oviedo, Spain.

[3]Radiochemistry Division, Bhabha Atomic Research Centre, Mumbai 400 085, India.

[4]Physical Sciences and Engineering Division, King Abdullah University of Science and Technology, Thuwal 23955-6900, Kingdom of Saudi Arabia.

Experimental Section

Materials and instrumentation

All chemicals were commercially available and used without further purification: phytic acid (PTA, Sigma–Aldrich,50 wt.% in H_2O), vanadyl sulphate (Sigma–Aldrich, 97%, analytical standard), vanadium pentoxide (Alfa Aesar, 99.2%), Phosphoric acid (PA, Sigma–Aldrich, 85 wt.% in H_2O), ammonia solution (Sigma–Aldrich, 28-30 wt.% in H_2O). X-ray diffraction (XRD) patterns were recorded on a Rigaku Mini Flex II diffractometer instrument using Cu–Kα radiation (λ = 1.5406 Å) at 35 kV and 30 mA. Transmission electron microscopy (HRTEM) was carried out using a JEOL-JEM-2010 2100F microscope operated at an accelerating voltage of 200 kV, equipped with a field emission gun (FEG) and an ultra-high-resolution pole-piece that provided a point-to-point resolution of 0.19 nm. This equipment was also equipped with a STEM system, which enabled high-angle annular dark field (HAADF) imaging. Prior to the analysis, the samples were dispersed in ethanol, sonicated and sprayed on a carbon-coated copper grids and then allowed to air-dry. The X-ray photoelectron spectroscopy (XPS) measurements were performed on a SPECS spectrometer equipped with a Phoibos 100 MCD analyzer and a monochromatized X-ray Al Kα (1486.6 eV). The energy calibrations were made against the C1s peak (set at 284.6 eV) to eliminate the charging of the sample during analysis.

High resolution spectra were taken with an energy pass of 30 eV and an energy step of 0.1 eV. Atomic Force Microscopy (AFM) was performed with a Nanotec Cervantes FullMode SPM microscope working in contact mode with gold coated silicon nitride tips. The powder sample was dispersed in ethanol and evaporated onto a silicon substrate for the characterization of the nanosheets morphology. N_2 adsorption-desorption measurements at 77 K were carried out using a Micromeritics ASAP 2020 instrument. Prior to the analysis, it was necessary to degas the samples (300-350 mg) at 125°C for 6 h. The specific surface areas were evaluated using the Brunauer–Emmett–Teller (BET) method and the pore distribution was calculated by BJH method. Positron annihilation lifetime spectroscopy (PALS) and coincidence Doppler broadening (CDB) measurements of the powder samples were carried out by immersing a positron source (activity ~ 10 micro curie) sealed in Kapton (thickness ~ 7 micrometer) films. It has been ensured that all the emitted positrons annihilate within the powder sample. PALS measurements were carried out using a fast-fast spectrometer consisting of two plastic scintillation detectors placed opposite to each other. The time resolution of the spectrometer is 285 ps and time calibration of the spectrometer is 0.0128 ns/channel. Each spectrum contains more than 1 million counts. The PALS spectra were analyzed using PALS fit.[1]

The CDB measurements were carried out using two HPGe detector placed at 180 degree to each other. Two HPGe detectors were used to record two annihilation photons E_1 and E_2 emitting from a single event. The Doppler broadening of annihilation photon due to momentum of annihilating electron is calculated as $\Delta E = E_1 - E_2 = cP_L$ where P_L is the longitudinal component of the positron-electron momentum along the direction of the detector and c is the velocity of light. In order to obtain the annihilating electron momentum distribution, coincidence events were selected in the range of E_t (1022 keV) < $2m_0c^2$ + 4.41 keV which resulted in the peak to background ratio equal to $>10^5$. The ratio curves were calculated by taking the ratio of area normalized momentum distribution curves of the samples with respect to a reference (Si crystal).[2]

Procedure for 2D β-$VOPO_4$ nanosheets (PTA-$VOPO_4$) preparation

In a typical synthesis of 2D β-$VOPO_4$ nanosheets, 2.4 grams of vanadyl sulphate ($VOSO_4$) was first dissolved in 60 mL water. Then, 3.3 grams of phytic acid solution (50 wt. % in H_2O) was added slowly to the $VOSO_4$ solution under vigorous stirring. Then, the PH of the mixture was adjusted to 6 by adding aqueous ammonia solution, followed by vigorous string for 2 h. Next, the resulting gel was transferred to a 100 mL Teflon-lined autoclave at 180 °C for 12 h. The suspension was cooled to room temperature, and then filtrated, washed with distilled water and dried at 80 °C for 24 hours, yielding a grey powder (PTA-derived VOP_{HT}). Subsequently, the resultant solid was loaded into a tube furnace, and heated to 550 °C for 6 h with a heating rate of 2 °C/min in the flowing air. The obtained yellow solid was β-$VOPO_4$ nanosheets (PTA-$VOPO_4$).

Procedure for 2D transition metal phosphate nanolayers ($FePO_4$, $CoPO_4$ and $NiPO_4$) preparation

In a typical synthesis of 2D $NiPO_4$ nanosheets, 7.5 mmol of Nickel (II) nitrate hexahydrate ($Ni(NO_3)_2 \cdot 6H_2O$) was first dissolved in 30 mL water. Then, 2.5 mmol of phytic acid solution (50 wt. % in H_2O) was added slowly to the $Ni(NO_3)_2$ solution under vigorous stirring. Then, the PH of the mixture was adjusted to 6 by adding aqueous ammonia solution, followed by vigorous string for 2 h. Next, the resulting gel was transferred to a 100 mL Teflon-lined autoclave at 180 °C for 12 h. The suspension was cooled to room temperature, and then filtered, washed with distilled water and dried at 80 °C for 24 h. Subsequently, the resultant solid was loaded into a tube furnace, and heated to 550 °C for 6 h with a heating rate of 2 °C/min in the flowing air. The obtained solid was $NiPO_4$ nanosheets. $FePO_4$ and $CoPO_4$ nanolayers were also prepared by a similar method using iron(III) nitrate nonahydrate ($Fe(NO_3)_3 \cdot 9H_2O$) and cobalt(II) nitrate hexahydrate ($Co(NO_3)_2 \cdot 6H_2O$), instead of $Ni(NO_3)_2$.

Procedure for phosphoric acid-derived *β*-$VOPO_4$ (PA-$VOPO_4$) preparation

According to the above similar procedure, the phosphoric acid-derived *β*-$VOPO_4$ (PA-$VOPO_4$) was prepared by using phosphoric acid (H_3PO_4), instead of phytic acid. Briefly, 2.4 grams of $VOSO_4$ and 1.7 grams of H_3PO_4 (85wt. %) were mixed with 60 mL of H_2O, and then adjusted to PH to 6 by adding aqueous ammonia solution. Subsequently, the suspension was transferred to an autoclave for crystallization at 180 °C for 12 h. The resulting solid was obtained by filtration and dry at 80 °C for 24 h (PA derived VOP_{HT}). Finally, the PA-$VOPO_4$ was obtained by the calcination of VOP_{HT} solid at 550 °C for 6 h in an air flow.

Preparation of vanadyl phosphate dihydrate ($VOPO_4 \bullet 2H_2O$)

The $VOPO_4 \bullet 2H_2O$ catalyst was prepared following the procedure reported by Ueda *et al.*[3] 5 grams of vanadium pentoxide (V_2O_5) was added to 30 mL phosphoric acid (H_3PO_4, 85 wt. %). Then, the mixture was refluxed at 110 °C for 16 h. Next, the bright-yellow precipitate was filtered off, washed several times with distilled water and acetone, and dried in an oven at 40 °C for 12h.

Preparation of vanadyl hydrogen phosphate hemihydrate ($VOHPO_4 \bullet 0.5H_2O$)

The $VOHPO_4 \bullet 0.5H_2O$ catalyst was prepared via the reduction of $VOPO_4 \bullet 2H_2O$ as precursor. In a typical synthesis, 2 grams of the resulting $VOPO_4 \bullet 2H_2O$ powder was added to 25 mL 2-butanol, followed by refluxing at 100 °C for 24h. After that, the suspension was filtered, washed with acetone and dried at room temperature for 24 h, yielding a light-blue $VOHPO_4 \bullet 0.5H_2O$ powder.

Preparation of vanadyl pyrophosphate [$(VO)_2P_2O_7$]

The $(VO)_2P_2O_7$ catalyst was prepared via direct calcination of $VOHPO_4 \bullet 0.5H_2O$. Briefly, 2 grams of $VOHPO_4 \bullet 0.5H_2O$ was calcined at 550 °C for 4h under nitrogen flow at the heating rate of 1°C/min. The obtained grey solid was confirmed to $(VO)_2P_2O_7$ by XRD pattern.

Procedure for catalytic experiments

The oxidative dehydrogenation of ethyl lactate to ethyl pyruvate was carried out in a fixed-bed quartz reactor with an internal diameter of 4 mm and a length of 300 mm. The catalyst bed was placed between quartz wool plugs in the middle of the reactor and the upper part was filled with quartz sands for preheating the ethyl lactate. For the *β*-$VOPO_4$ nanosheets (PTA-$VOPO_4$) catalysts, 0.5 grams of catalyst (20–25 mesh) was loaded in the reactor wih the catalyst bed thickness of ca. 2ml (diluted with 2-25 mesh quartz sands). Next, the catalyst was pretreated in an air flow at 300 °C for 1h to eliminate any surface moisture and then cool to reaction temperature. After that, ethyl lactate was injected into the reactor at a rate of 3 mL/h using a HPLC pump and using air as the carrier gas and terminal oxidant (under atmosphere pressure). After each reaction period of 2 h, the products were quenched and collected in an ice trap, then analyzed by gas chromatography (GC) equipped with a flame ionization detector (FID) and Stabilwax-DA capillary column (30 m × 0.32 mm × 3.00 μm). And the effluent gas was analyzed by an online GC fitted with a MoSieve 5A column and a TCD detector. We could detect CO_x only in trace amounts under our main reaction conditions. Carbon balance (mol%) was calculated by summing up the unreacted ethyl lactate and the total quantities of detected and calibrated products.

The ethyl lactate (EL) conversion, product selectivity and pyruvate yield were calculated accroding to the following equations:

$$EL\ conversion\ (\%) = \frac{moles\ of\ ELfed\ into\ the\ reactor - moles\ of\ unreacted\ EL}{moles\ of\ EL\ fed\ into\ the\ reactor} \times 100\ \% \tag{1}$$

$$Product\ selectivity\ (\%) = \frac{moles\ of\ carbon\ atoms\ in\ the\ product}{moles\ of\ carbon\ in\ all\ detected\ products} \times 100\ \% \tag{2}$$

$$Pyruvate\ yield\ (\%) = \frac{moles\ of\ pyruvate\ produced}{moles\ of\ ELfed\ into\ the\ reactor - moles\ of\ unreacted\ EL} \times 100\ \% \tag{3}$$

The specific-mass productivity of pyruvate ($g_{\mathrm{pyruvate}}/g_{\mathrm{catalyst}}$/hour)

$$= \frac{grams\ of\ EP\ produced\ per\ hour\ in\ the\ reactor\ (g_{\mathrm{pyruvate}}/hour)}{grams\ of\ catalyst\ in\ the\ reactor\ (g_{\mathrm{catalyst}})} \tag{4}$$

The area-specific productivity of pyruvate ($g_{\mathrm{pyruvate}}/m^2$/hour)

$$= \frac{grams\ of\ pyruvate\ produced\ per\ hour\ in\ the\ reactor\ (g_{\mathrm{pyruvate}}/hour)}{surface\ area\ of\ the\ catalyst\ in\ the\ reactor\ (m^2)} \times 100\ \% \tag{5}$$

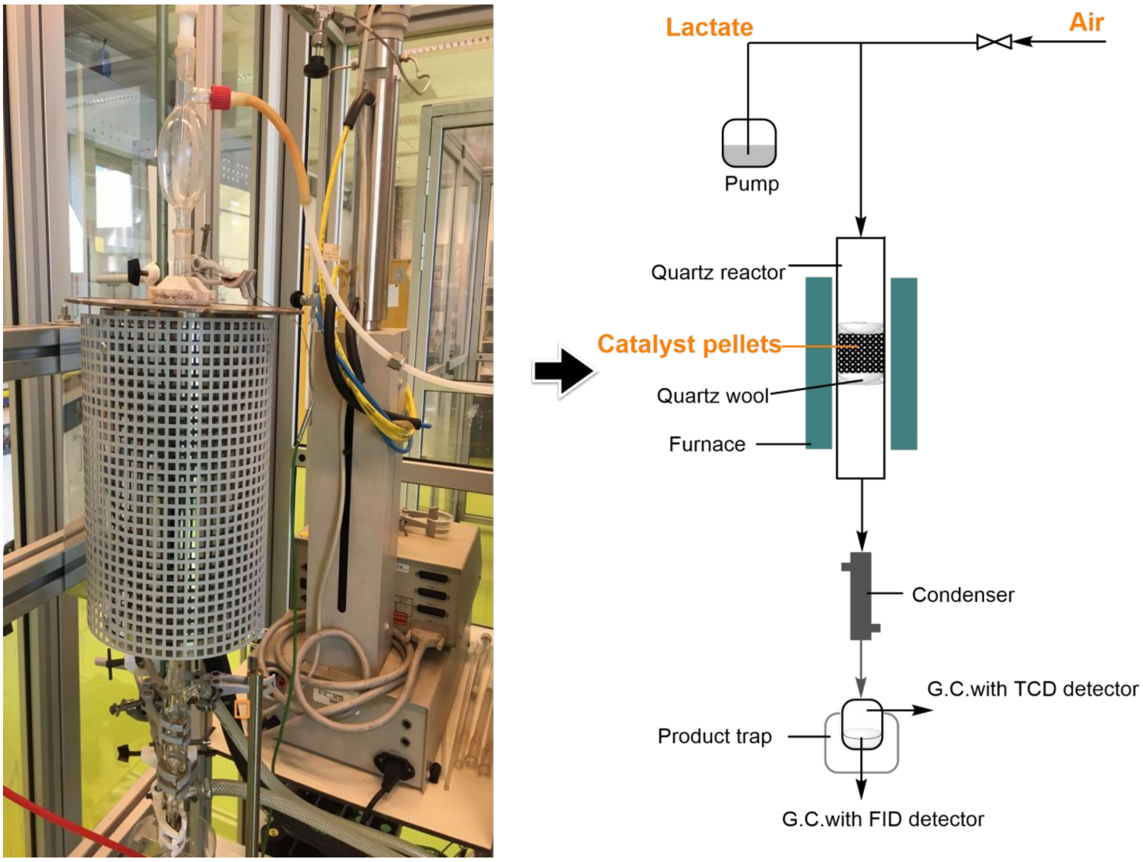

Figure S1. The fixed-bed flow reactor in which the ethyl lactate to pyruvate was conducted (left) and a schematic diagram of the reactor set-up (right).

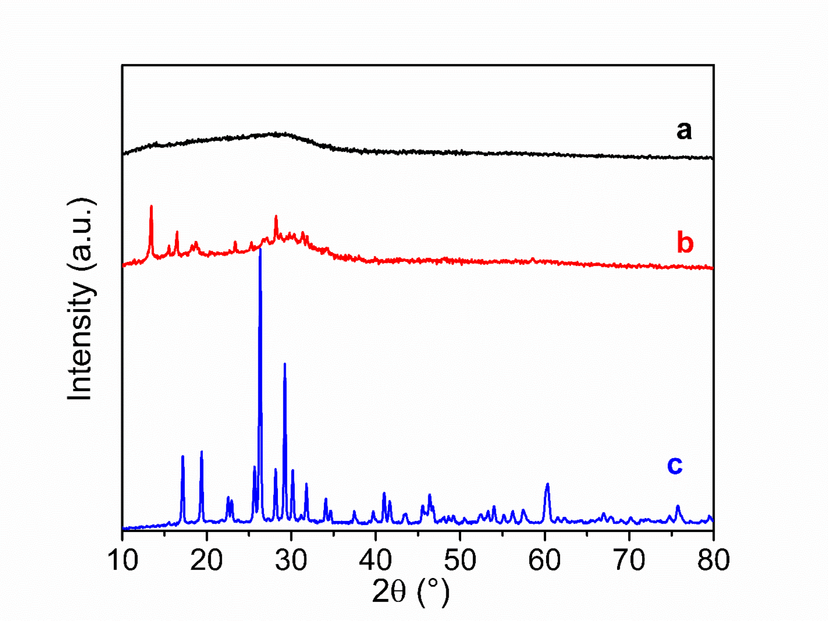

Figure S2. X-ray diffraction pattern of (a) vanadium-PTA coordination precursors, (b) VOP@C (after hydrothermal treatment) and (c) *β*-$VOPO_4$ nanosheets (calcined at 550 °C for 4h). Drying of the vanadium-PTA coordination precursors yielded amorphous structure. After hydrothermal treatment, the as-made solids were converted into vanadium phosphates (VOP) and their organic segments were carbonized into a carbon framework, giving VOP@C hybrids. Subsequent calcination removed the carbon and crystallized the material into pure orthorhombic *β*-$VOPO_4$ phase.

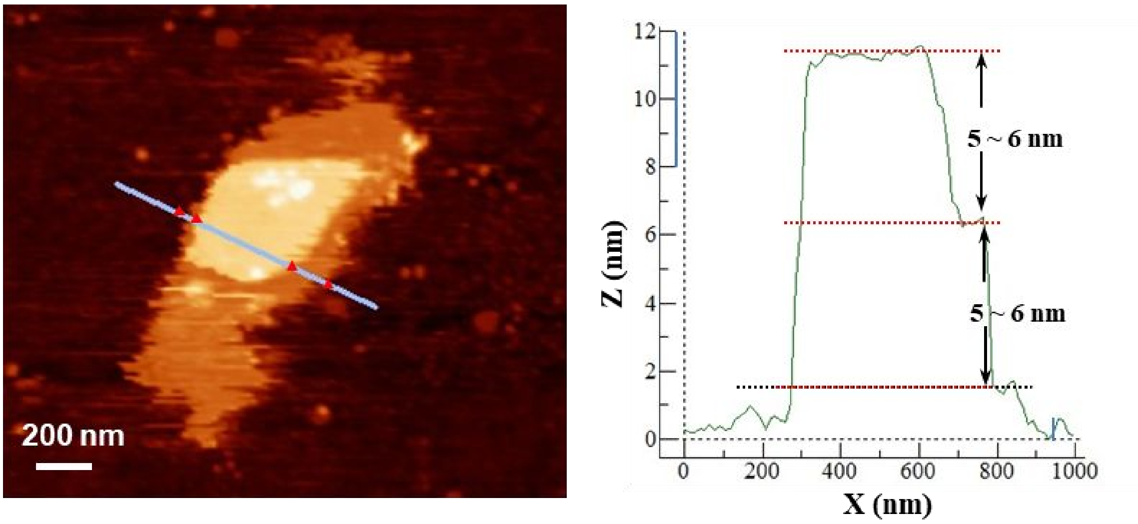

Figure S3. Representative AFM image of few-layer *β*-$VOPO_4$ nanosheets (left) and the corresponding thickness of nanosheets derived from AFM measurement (right).

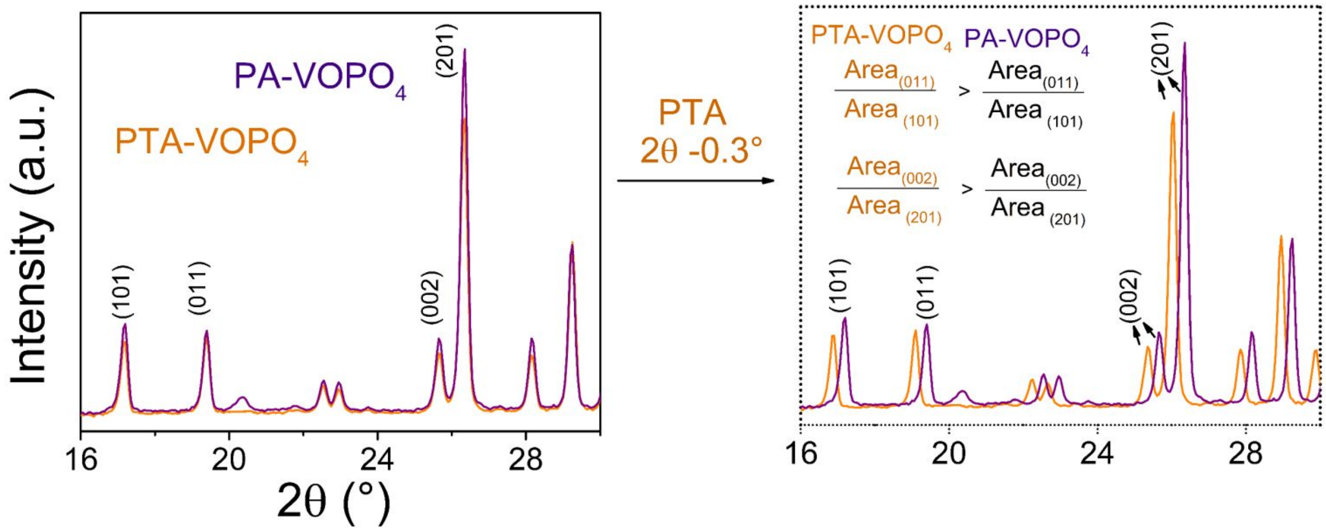

Figure S4. Comparison of the X-ray diffraction patterns of PTA-VOPO$_4$ and PA-VOPO4 (left). To better differentiate the XRD patterns, the X-axis of PTA pattern is shifted from 2θ to (2θ-0.3 °), where area represents the XRD integrated intensity of the corresponding diffraction peak (right).

Table S1. Atomic ratios of PTA-$VOPO_4$ calculated from the energy dispersive X-ray (EDX) analysis.

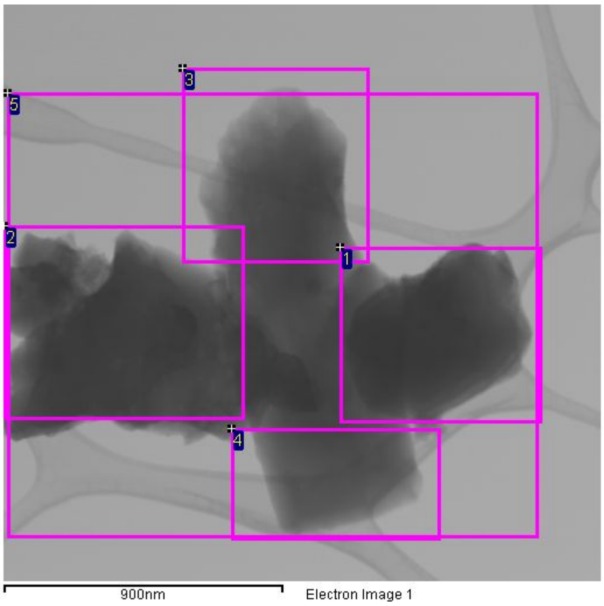

Spectrum	V (atomic %)	P (atomic %)	O (atomic %)	V/P
1	22.95	24.79	52.26	0.93
2	27.23	28.64	44.12	0.95
3	22.46	26.53	51.01	0.85
4	19.66	22.33	58.02	0.88
5	23.12	26.26	50.63	0.88
Mean	23.084	25.71	51.208	0.90

Table S2. Atomic ratios of PA-$VOPO_4$ calculated from the energy dispersive X-ray (EDX) analysis.

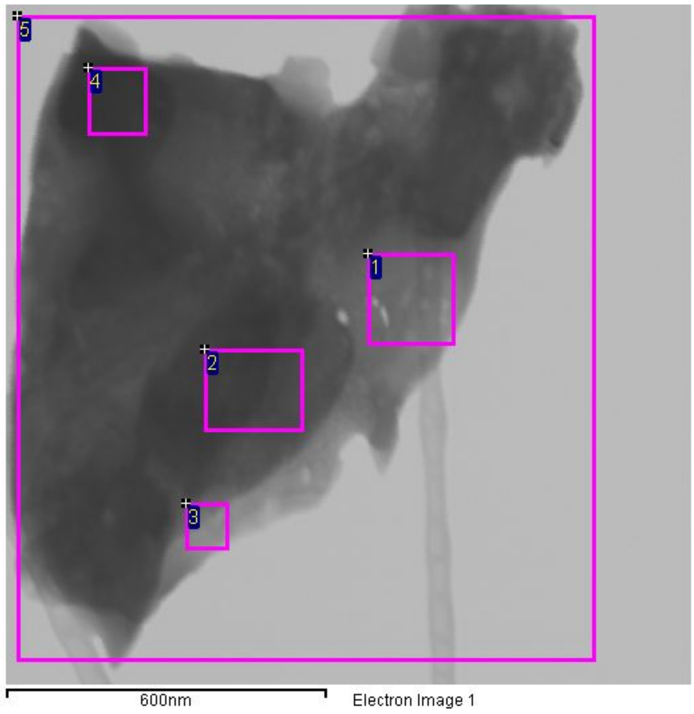

Spectrum	V (atomic %)	P (atomic %)	O (atomic %)	V/P
1	55.4	38.75	5.85	1.43
2	45.53	33.18	21.28	1.37
3	49.89	34.18	15.93	1.46
4	37.89	26.78	35.33	1.41
5	40.03	29.67	30.3	1.35
Mean	45.75	32.51	21.74	1.41

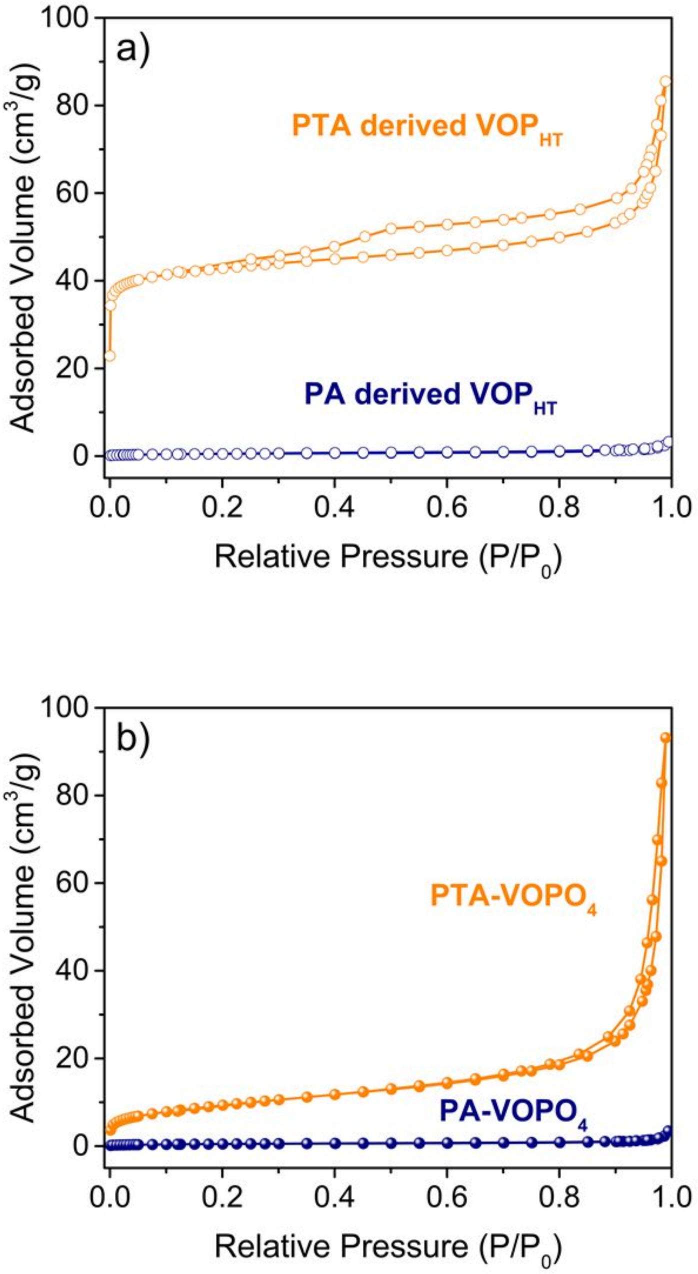

Figure S5. Nitrogen adsorption–desorption isotherms of (a) PTA-VOP$_{HT}$ and PA-VOP$_{HT}$ (after hydrothermal treatment) and (b) PTA-VOPO$_4$ and PA-VOPO$_4$.

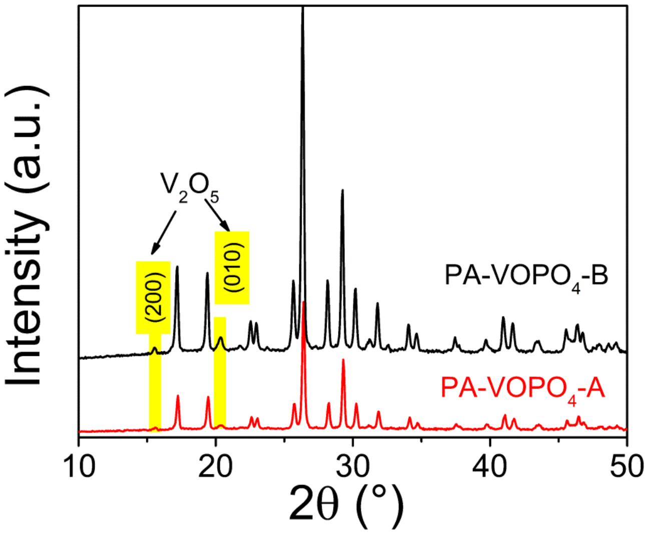

Figure S6. X-ray diffraction patterns of phosphoric acid-derived $VOPO_4$ (PA-$VOPO_4$) with $VOSO_4$/PA molar ratios of 0.5 and 0.8 prepared under otherwise identical conditions: PA-$VOPO_4$-A (molar ratio=0.5) and PA-$VOPO_4$-B (molar ratio=0.8).

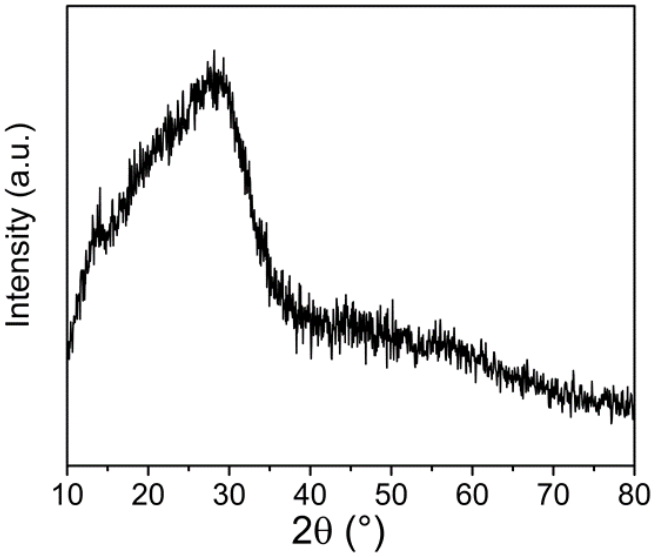

Figure S7. X-ray diffraction pattern of amorphous PTA-derived $VOPO_4$ without the hydrothermal treatment (vanadium-PTA hybrids were directly calcined at 550 °C for 6h under air atomosphere).

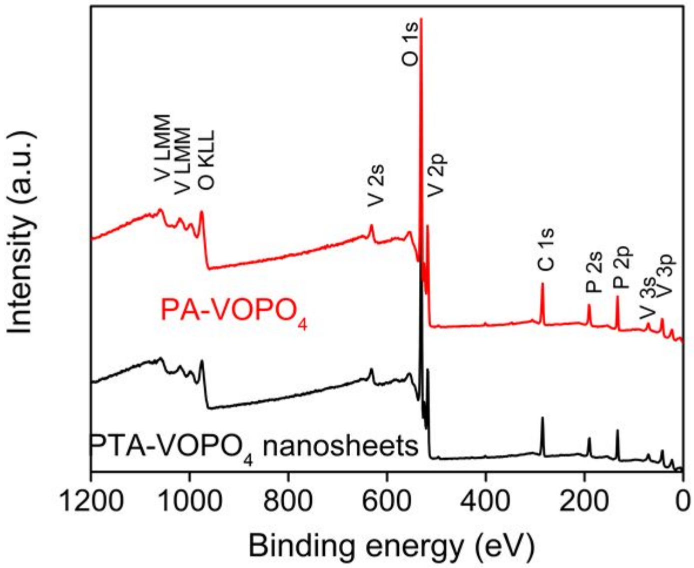

Figure S8. The full XPS survey spectra of PTA-$VOPO_4$ nanosheets and bulk PA-$VOPO_4$ (Note: The vanadyl phosphates are carbon-free, as all the resulting $VOPO_4$ samples are calcined at 550 °C for 6 h in an air flow. The samples were measured on the top of shaped graphene sheets, as the energy calibrations were made against the C1s peak to eliminate the charging of the sample during analysis).

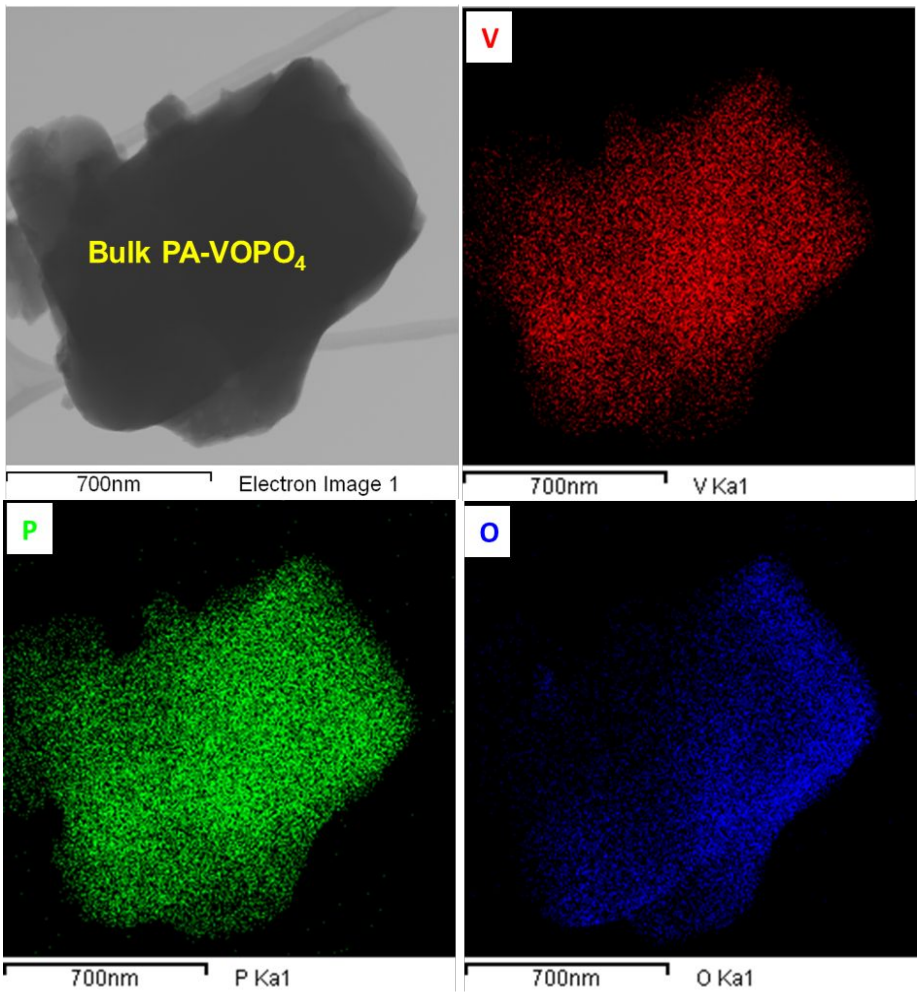

Figure S9. Representative STEM image and corresponding elemental mappings of V, P, and O in bulk PA-VOPO$_4$.

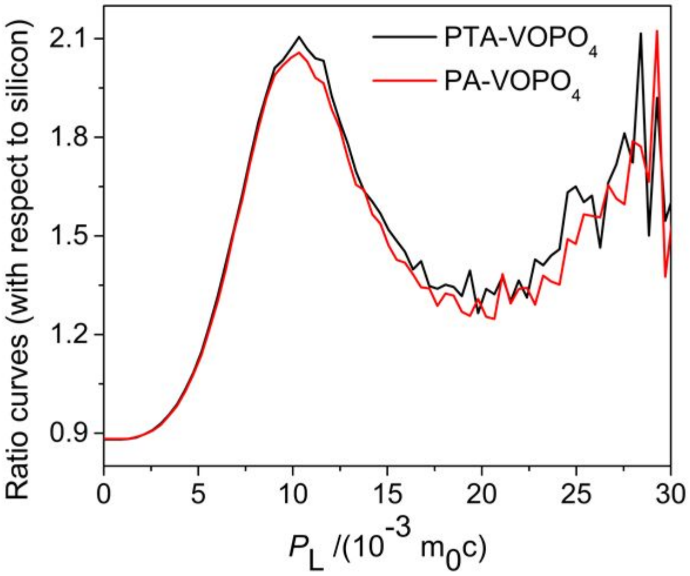

Figure S10. Ratio curves of the samples with respect to a reference (Si) measured using coincidence Doppler broadening spectrum.

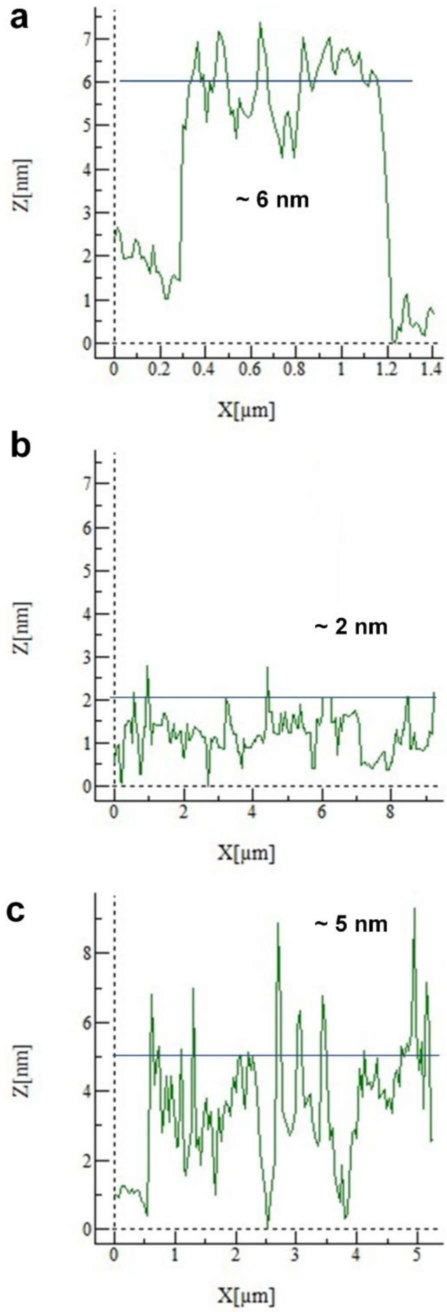

Figure S11. The height profles of various phytic acid-derived phosphate nanosheets derived from AFM measurement in Figure 5: (**a**) $NiPO_4$ nanosheets, (**b**) $CoPO_4$ nanosheets and (**c**) $FePO_4$ nanosheets,

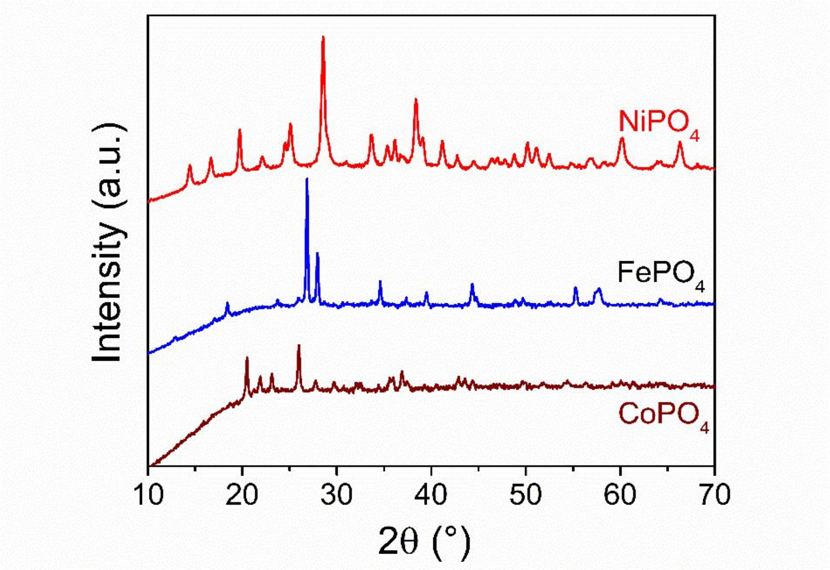

Figure S12. X-ray diffraction pattern of various phytic acid-derived phosphates.

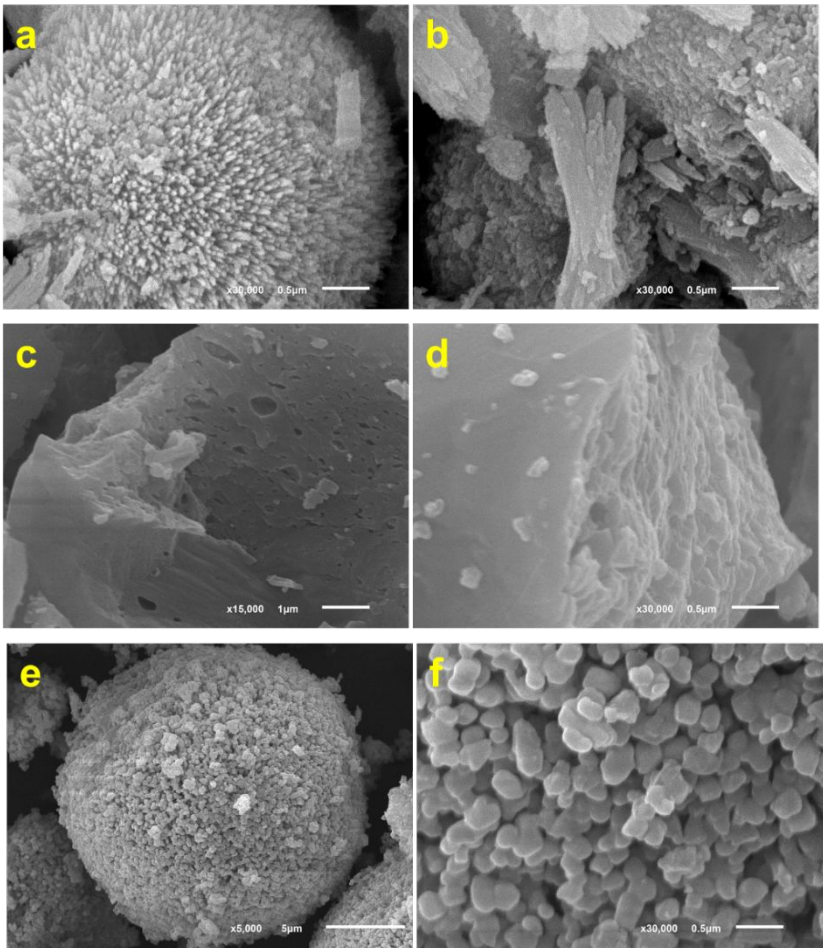

Figure S13. The SEM images of the $NiPO_4$(a-b), $CoPO_4$ (c-d) and $FePO_4$ (e-f), respectively.

Table S3. Atomic ratios of $NiPO_4$ calculated from the energy dispersive X-ray (EDX) analysis.

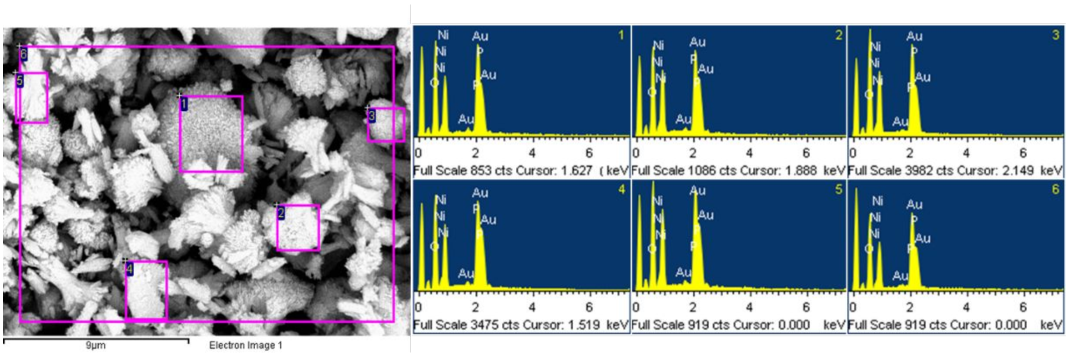

Spectrum	Ni (atomic %)	P (atomic %)	O (atomic %)	Ni/P
1	13.18	11.45	75.37	1.2
2	11.86	10.88	77.27	1.1
3	11.29	10.28	78.43	1.1
4	12.33	11.03	76.64	1.1
5	11.02	10.68	78.3	1.0
6	15.46	11.74	72.81	1.3
Mean	12.52	11.01	76.47	1.1

Table S4. Atomic ratios of $CoPO_4$ calculated from the energy dispersive X-ray (EDX) analysis.

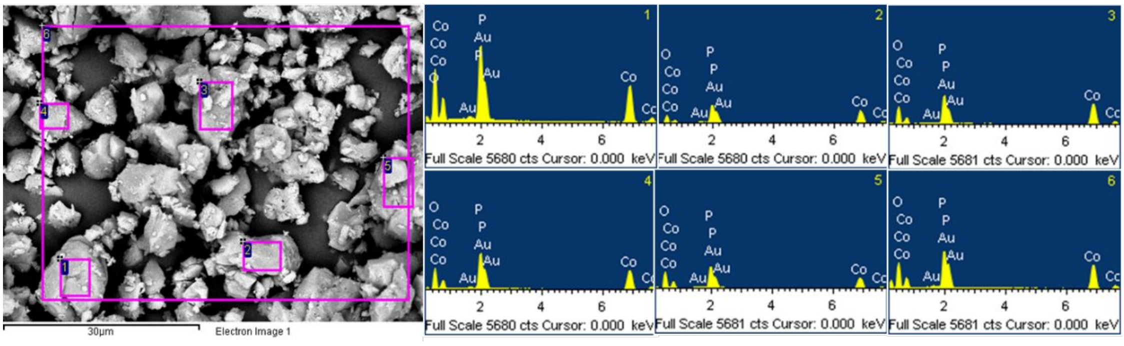

Spectrum	Co (atomic %)	P (atomic %)	O (atomic %)	Co/P
1	15.05	14.47	70.48	1.0
2	25.98	18.49	55.53	1.4
3	22.40	15.02	62.58	1.5
4	18.82	16.19	64.99	1.2
5	15.69	14.06	70.25	1.1
6	18.66	13.79	67.55	1.4
Mean	19.43	15.34	65.23	1.3

Table S5. Atomic ratios of $FePO_4$ calculated from the energy dispersive X-ray (EDX) analysis.

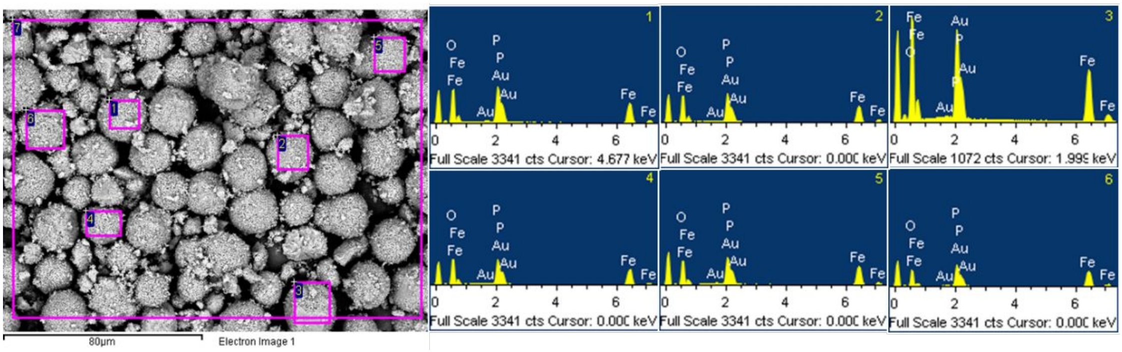

Spectrum	Fe (atomic %)	P (atomic %)	O (atomic %)	Fe/P
1	13.3	11.92	74.78	1.1
2	13.65	11.62	74.73	1.2
3	12.09	11.05	76.86	1.0
4	13.24	11.15	75.61	1.1
5	15.72	12.29	71.99	1.2
6	18.45	13.25	68.3	1.3
Mean	14.4	11.88	73.7	1.2

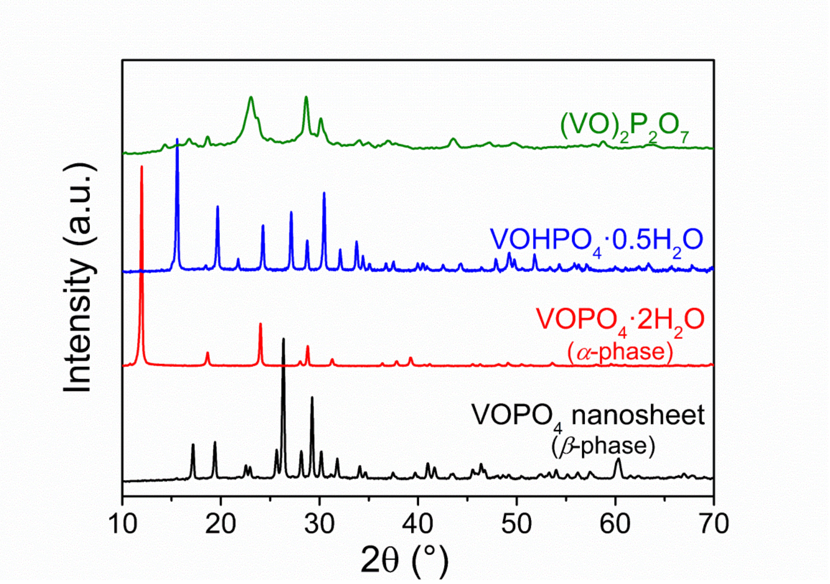

Figure S14. X-ray diffraction patterns of VOP catalysts: 2D β-$VOPO_4$ nanosheets, $(VO)_2P_2O_7$, $VOHPO_4 \cdot 0.5\ H_2O$ and $VOPO_4 \cdot 2H_2O$.

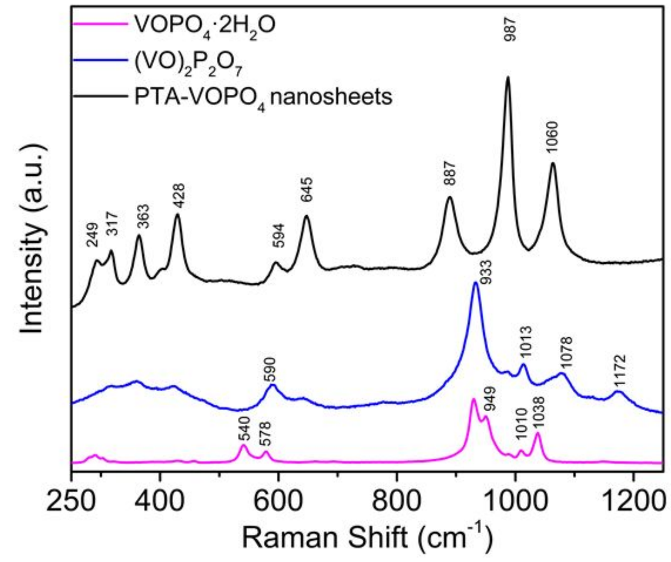

Figure S15. Raman spectra of VOP catalysts: 2D β-$VOPO_4$ nanosheets, $(VO)_2P_2O_7$ and $VOPO_4 \cdot 2H_2O$.

Table S6. Effect of WHSV on aerobic oxidation of ethyl lactate with air to ethyl pyruvate.[a]

$WHSV_{EL}$ (h^{-1})	EL Conv. (mol%)	Product selectivity (mol%)							Pyruvates yield (mol%)	Carbon balance (%)[c]
		Pyruvates	Acetaldehyde	EtOH	HAc	Ethyl acetate	Propionic acid/ethyl propionate	Others[b]		
1	95.4	71.3	2.4	4.8	16	1.3	1.8	2.4	68	96
2	93.0	71.9	3.6	5.2	12.8	1.7	2.0	2.8	66.9	97.2
3	89.5	82.1	2.2	3.6	7.7	1.1	1.4	1.9	73.7	98.1
4	83.9	83.9	4.1	5.2	2.9	0.8	1.3	1.8	70.4	98.2
6	77.1	81.8	3.9	5.4	4	1.0	1.7	2.2	63.1	97.8
8	63.6	85.9	5.6	2.5	3.7	0.5	0.8	1	49.5	99

[a] Reaction temperature: 300 °C; 1 atm; Air flow rate: 2.25L/h. EL-ethyl lactate; Pyruvates: ethyl pyruvate + pyruvic acid; EtOH-ethanol; HAc-acetic acid; Detected product selectivity (mol%) = (moles of carbon atoms in the product)/ (moles of carbon in all detected products) ×100 %. [b] Selectivity for "others" (mol %) = 100 − ∑ (selectivity for each listed product). [c] Carbon balance (mol%) was calculated by summing up the unreacted ethyl lactate and the total quantities of detected products.

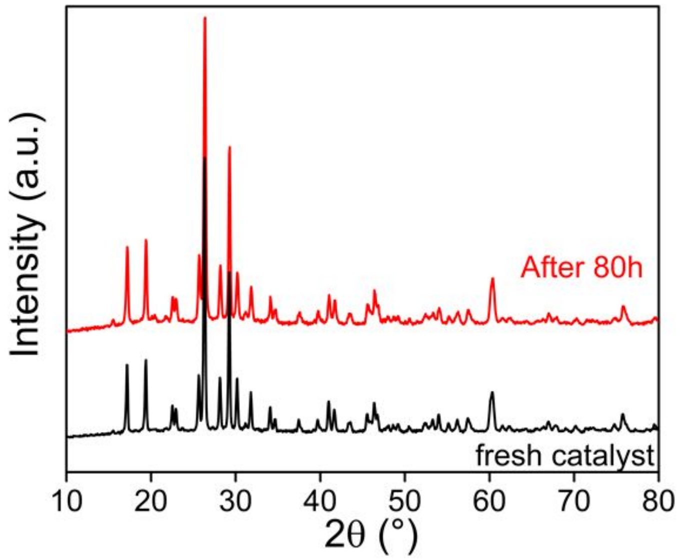

Figure S16. X-ray diffraction pattern of the regenerated *β*-VOPO$_4$ nanosheets.

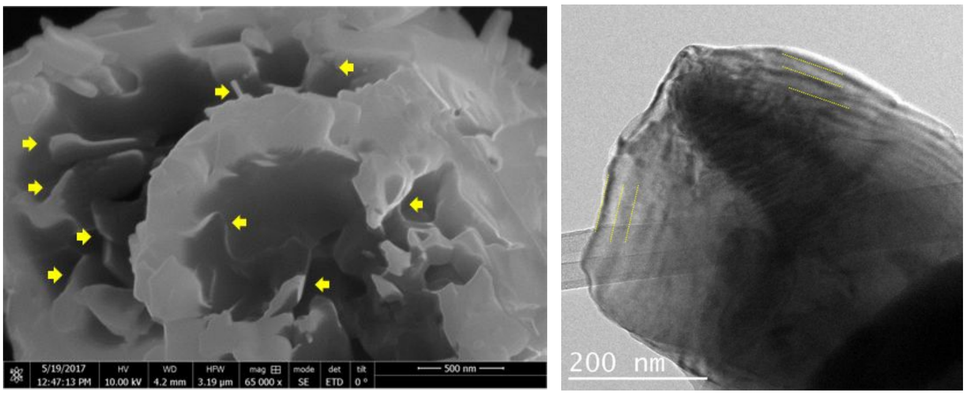

Figure S17. SEM and TEM images of the regenerated *β*-VOPO$_4$ nanosheets.

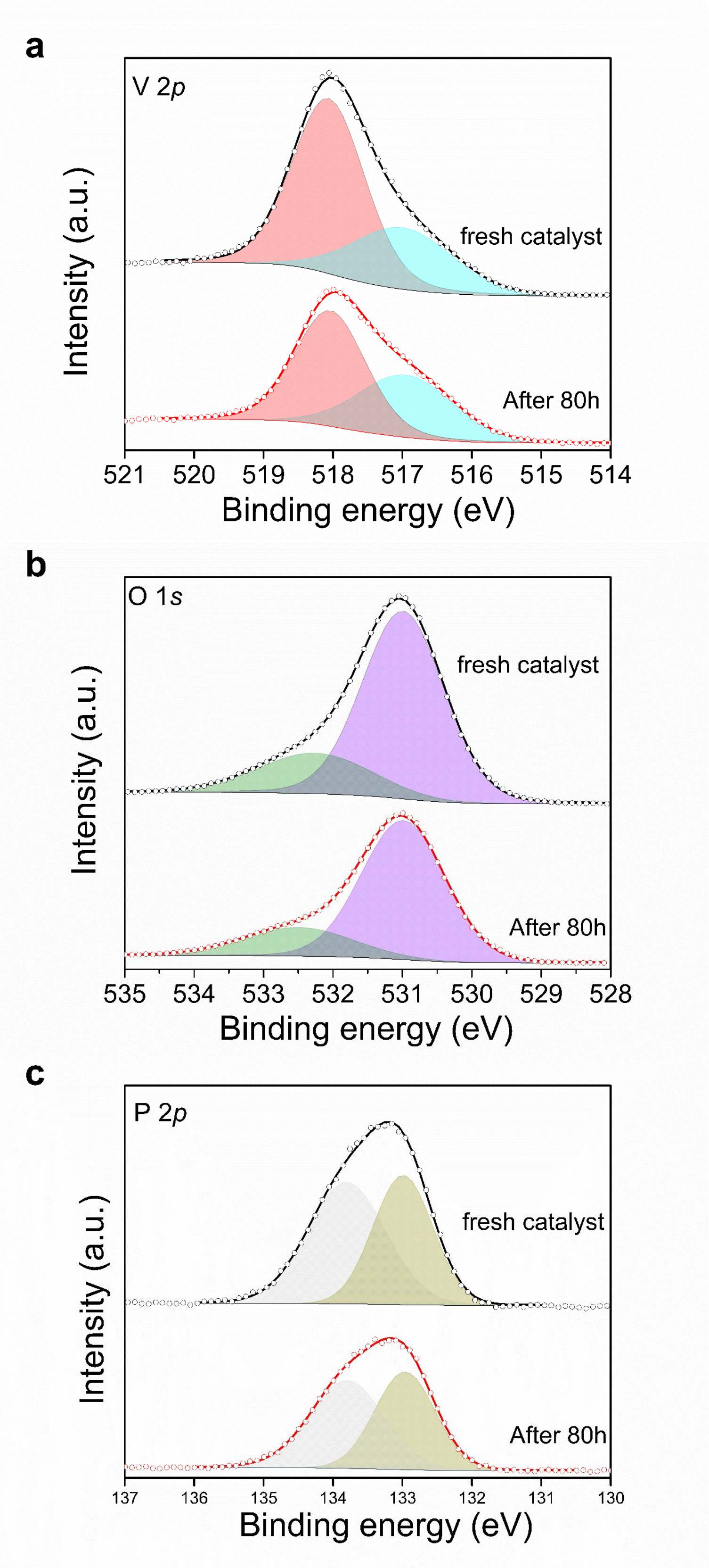

Figure S18. XPS spectra of the regenerated *β*-$VOPO_4$ nanosheets (a) high resolution V2*p* spectra, (b) high resolution O1s spectra and (c) high resolution P 2*p* spectra.

References

(1) Kirkegaard, P. & Eldrup, M. Positronfit extended: A new version of a program for analysing position lifetime spectra. *Comput. Phys. Commun.* **1974**, *7*, 401-409.

(2) Sharma, S. K.; Sudarshan, K.; Maheshwari, P; Dutta, D.; Pujari, P. K.; Shah, C. P.; Kumar, M. and Bajaj, P. Direct evidence of Cd vacancies in CdSe nanoparticles: positron annihilation studies. *Eur. Phys. J. B* **2011**, *82*, 335.